

JET-GAS INTERACTION IN MKN 78 – III: GAS DYNAMICS AND JET PROPERTIES

M. WHITTLE¹, J.D. SILVERMAN^{1,2}, D.J. ROSARIO¹, C.H. NELSON³, A.S. WILSON^{4,5}*To appear in Astronomical Journal*

ABSTRACT

We extend our study of the Seyfert galaxy Markarian 78, focusing on the dynamics of the emission-line region and the properties of the bipolar radio-emitting jet. New high dispersion STIS spectra at four slit locations reveal a rich [OIII] λ 5007 velocity field. We study three distinct regions: an inner western knot (W-knot) of modest kinematic disturbance; an eastern fan-like region (E-fan) with widely split lines; an outer western lobe (W-lobe) with multiple high-velocity components. The data support the basic picture introduced in Paper I: the radio source interacts with ionized gas, accelerating and dispersing it.

We measure a number of (projected) properties: each region contains $\sim 10^6 M_{\odot}$ of ionized gas with low filling factor and high ($\sim 50\%$) local covering factor; the regions' crossing times confirm our suggestion from Paper I of an increasing interaction age: W-knot is youngest (~ 0.4 Myr), E-fan is intermediate (~ 4 Myr) and W-lobe is oldest (~ 8 Myr). Energy within the regions is divided in the following (relative) way: intercepted nuclear UV ($\times 1000$); emission line ($\times 1000$); kinetic ($\times 1$); relativistic ($\times 1$); expansion ($\times 1$); and radio ($\times 0.3$). These confirm (a) that nuclear UV luminosity dominates the overall energy budget; (b) that line emission is powered by nuclear UV radiation and not by shocks (as found in Paper II); and (c) that acceleration of the ionized gas is probably associated with the radio source. The pressure of the relativistic component nicely matches (a) that expected of the host galaxy ISM; (b) the ionized gas, including an $\sim r^{-1}$ radial decrease; and (c) that needed to drive lobe expansion into the ISM at the local [OIII] velocity. The high momentum of the ionized gas places strict limits on the accelerating force: radiation pressure and internal (static) relativistic pressure are probably too weak (by factors $\sim \times 3$), suggesting the need for a dynamical pressure to drive the ionized gas.

We next evaluate properties of the radio (jet) flow, using three important assumptions: (1) the jet momentum flux (integrated over the region lifetime) can be estimated from the momentum of the ionized gas; (2) the jet luminosity (integrated over the region lifetime) can be estimated from the energy stored in the radio lobe; and (3) the radio lobe contains relativistic and thermal gas in rough pressure balance. For each region we obtain similar properties for the jet flow: luminosity $\sim 10^{40.5}$ erg s⁻¹; momentum flux $\sim 10^{33.5}$ dyne; velocity ~ 1 –few times the ionized gas velocity; dynamical (ram) pressure a few times the static (relativistic) pressure; particle density ~ 0.1 – 5 cm⁻³; transonic Mach numbers ~ 2 – 5 ; temperature $\sim 10^6$ K; and $\dot{M} \sim 0.1 M_{\odot}$ yr⁻¹. Compared to radio loud AGN jets, our jet is weak, slow, and dense, with its inertia and luminosity both dominated by the thermal component, *not* the relativistic component. Nevertheless, we feel the jet's properties are quite plausible: its ram pressure can accelerate the ionized gas to the observed velocities; its density is consistent with entrained ISM; its low Mach number confirms that entrainment is efficient, and accounts the overall FR-I morphology; its synchrotron efficiency matches jets in other classes of AGN ($L_j/L_{rad} \approx 1$ –few %); and over the region lifetime the jet's thermal payload can provide the low density high filling factor phase of the radio lobes.

Our jet differs markedly from jets whose properties are derived assuming the emission lines are both powered by and accelerated by fast radiative shocks. Such assumptions lead to a jet which has $\sim 10^3$ times the power, $\sim 10^2$ times the momentum flux, much higher velocity and temperature, and much lower density and synchrotron efficiency. We argue that our starting assumptions are more plausible, as are our derived jet properties.

Finally, we place constraints on the properties of the nuclear (sub-pc) jet by demanding that it have the same momentum as the kpc-scale jet, at least as much power, and radio emission consistent with the weak unresolved radio core. We find that neither pure relativistic nor pure thermal jets are viable — it seems the jets of radio quiet AGN may be created with both thermal and relativistic components. At this time, we cannot estimate their relative amounts.

Subject headings: ISM: jets and outflows — galaxies: individual (Mkn 78) — galaxies: jets — galaxies: kinematics and dynamics — galaxies: Seyfert

¹ Astronomy Department, University of Virginia, Charlottesville, VA 22903; djr4t@virginia.edu, dmw8f@virginia.edu, jds6h@virginia.edu

² Current address: Harvard-Smithsonian Center for Astrophysics, Cambridge MA 02138

³ Physics and Astronomy, Drake University, Des Moines, IA 50311-4505; charles.nelson@drake.edu

⁴ Astronomy Department, University of Maryland, College Park, MD 20742; wilson@astro.umd.edu

⁵ Adjunct Astronomer, Space Telescope Science Institute.

1. INTRODUCTION

This is the third paper in a series on the Seyfert galaxy Markarian 78. Our overall aim is to understand how bipolar radio-emitting jet flows interact with the surrounding ISM. Mkn 78 was chosen because it stood out in a survey of Seyferts which had linear radio sources, as one of the clearest examples of a jet-ISM interaction (Whittle et al. 1988). We hope, of course, that what we find in the case of Mkn 78 is more widely true of AGN in general, at least those classified as radio quiet (such as Seyferts).

In Paper I (Whittle & Wilson 2004) we constructed a qualitative picture of the jet-gas interaction, drawing upon continuum, emission line and radio images, as well as limited spectroscopy. In Paper II (Whittle et al. 2004) we focussed on the ionization mechanisms acting on the line-emitting gas. Given recent interest in the possible importance of shock related ionization, particularly in jet-dominated AGN (e.g. Dopita & Sutherland 1995), we looked hard for shock-related emission-line signatures, finding essentially none. Instead, we confirmed the dominance of nuclear UV photoionization, including the likely presence of both optically thin and thick gas, as suggested by Binette, Wilson, & Storchi-Bergmann (1996). Our negative result in this optimum case calls into question the importance of shock-related ionization in other Seyferts, and possibly all AGN. In this paper we attempt to combine all our observations to construct a detailed physical picture of both the emission line regions and the jet flow. Given our result from Paper II, however, we choose *not* to employ constraints derived from shock physics in our analysis.

Previous work on the physical properties of jet flows in radio quiet AGN has been quite limited. While a number of studies consider how jets propagate into an emission line region and interact with its clouds, most assume the jet properties as an input, and explore the consequences. Our aim is quite different. We are starting from an observational dataset and our intention is to *derive* the jet properties from that dataset using, hopefully, plausible assumptions. One of the few previous studies of this kind was that of Bicknell et al. (1998), and we rely heavily on that work and their approach. At the time of that study, the importance of shocks was undecided, and they chose to use shock physics to help constrain two fundamental jet properties: the jet's luminosity was taken to be roughly equal to the emission line luminosity (since emission lines, they assume, come from jet driven shocks); and the jet's momentum flux was derived assuming the emission line Doppler velocities are roughly equal to the shock velocities arising from the jet's impact on ionized gas clouds. These assumptions yield high power, high momentum, low density but fast jets.

While our approach follows that of Bicknell et al., we make two very different assumptions when deriving the jet's luminosity and momentum flux. As we shall show, this leads to a radically different kind of jet, one which is much weaker, slower, and denser. We feel that this weaker jet is more plausible, and its properties may signify one of the key difference between radio loud and radio quiet AGN. We also wish to encourage those building theoretical models to consider weaker but denser jets of the kind derived here.

The layout of this paper is as follows: observations and

measurements (principally of the new STIS data) are given in §2 and §3; a descriptive overview of the features identified is given in §4 together with a brief heuristic interpretation; in §5 we begin evaluating a number of physical properties of the line-emitting and radio-emitting regions, and these properties are used in §6 to derive the properties of the jet flow; in §7 we review our assumptions and compare our results with those of Bicknell et al.; in §8 we try to constrain the properties of the jet on much smaller scales; in §9 we try to place our results into a broader framework, drawing on other work in the area; finally in §10 we itemize our conclusions. We also give two appendices: the first gathers a wide range of simple relations that we use throughout the paper; and the second presents a dispersed but slitless STIS image of Mkn 78, and discusses the advantages and disadvantages of this kind of data compared with slit data.

2. OBSERVATIONS

The observational dataset we use in this paper was introduced in Papers I and II, and these papers should be consulted for more details. Briefly, HST images include a high S/N ratio PC [OIII] line image, several lower S/N ratio PC and FOC continuum images, two STIS CCD wide band images, a STIS MAMA near UV image, a NICMOS F160W image, and a deep 3.6cm VLA radio image. HST spectra were acquired using both FOS and STIS. Our FOS data included full optical coverage (G400H, G570H, G780H: 3200 – 8000 Å) in five apertures, and more limited coverage (G570H: 4570 – 6820 Å) in a further five. Our more recent STIS data includes full optical and UV coverage (G140L, G430L, G430M, G750M) at four slit positions, three parallel to the radio axis and one diagonal crossing the strongest features and the true (heavily reddened) nucleus. Figure 1 in Paper II shows all FOS and STIS aperture locations, while Figures 6 in Paper I and 2 in Paper II show the full FOS and STIS datasets. Figure 1 is adapted from Paper I Figures 4 and 9 and shows the VLA 3.6cm map (white contours) superposed on the [OIII] HST image (black contours), with regions labelled as in Paper I.

Of principal interest in the present paper is the high dispersion G430M STIS dataset which spans the H β and [OIII] λ 4959, 5007 lines at 0.28 Å pix⁻¹. Figure 2 shows the continuum subtracted G430M data for the [OIII] λ 5007 line for all four slits, with slit locations shown superposed on the PC [OIII] image and VLA 3.6cm radio image to the left and right of the spectra. As described in Paper II, slit location was confirmed by comparing the flux distributions in the spectroscopic and imaging data. A brief inspection of Figure 2 verifies that where a slit crosses an [OIII] feature, a spectral feature is also seen.

3. DYNAMICAL MEASUREMENTS

To ascertain the all important dynamical properties such as ionized gas momentum and kinetic energy, we need to measure and combine a number of quantities. Measurement of the basic parameters, including emission line fluxes and kinematics, were described in §3 of Paper II. Here we focus only on the quantities needed to evaluate the dynamical parameters. Figures 3 *a – d* show most of these quantities as a series of sub-panels for each of the four slits.

Note that all sub-panels in these plots are marked in arcseconds along the top and STIS pixels along the bottom, with the position of the nucleus marked by the vertical dotted line (STIS pixel 87.5 in our figures, pixel 600.5 in the original data frames).

The top panel in each figure shows the slit position superposed on the PC [OIII] image, while panel 2 shows the STIS G430M spectral data for the $\lambda 5007$ line. Panels 3 and 4 show the C80 and FWHM parameters measured from the [OIII] $\lambda 5007$ profile, which indicate the (projected) bulk velocity and internal dispersion velocity of the ionized gas. C80 is given relative to the systemic velocity (heliocentric 11052 km s⁻¹ taken from a ground based extended rotation curve; Whittle et al 1988). When more than one velocity component is visible, each has been measured and given a different symbol, with filled circle, open square, and open circle going from low to high velocity. Panel 5 shows the extinction A_V in magnitudes, while panel 6 shows the [SII] $\lambda 6731/6717$ ratio with corresponding (log) electron density scale on the right hand y-axis, with conversion taken from Osterbrock (1989). The dashed lines indicate the low and high density limits. Panel 7 shows the [OIII] $\lambda 5007$ flux in erg s⁻¹ cm⁻² pix⁻¹ along the slit, both before and after reddening corrections (with additional offset by $\times 10$ for clarity). The H β flux distribution (not shown) looks quite similar, though with larger error bars.

From these observed quantities we derive several physical quantities. Using the (reddening corrected) H β luminosity and electron density we derive a surface mass density, in M_\odot pc⁻², which is shown in panel 8 (1 pixel covers 1275 pc² or 0.0025 arcsec²). This is combined with the projected bulk velocity, C80, to yield a momentum, in dyne sec pc⁻², plotted in panel 9. Finally, panel 10 shows the projected kinetic energy, in erg pc⁻², where the velocity is chosen to be the quadrature sum of the projected bulk velocity, C80, and the velocity dispersion, $\sigma = \text{FWHM}/2.36$. Simple relations for these and other important quantities are given in Appendix A.

3.1. Error estimates

Error estimates for the measured quantities were described in §3 of Paper II. Estimating errors for the derived quantities is not straightforward, principally because highly non-linear functions (e.g. reddening corrections using the Balmer decrement; electron density using the [SII] ratio) prevent a simple propagation of error analysis. We therefore adopted a Monte Carlo (bootstrap) method to evaluate the errors. All derived quantities are evaluated 10⁶ times, each time using input quantities chosen randomly from Gaussian distributions whose means and sigmas correspond to the measurement values and errors. In this way the distribution of the derived quantity is produced, and from its interpercentiles we estimate an equivalent 2σ (95%) error. It is these errors which are plotted in Figs 3 a–d.

While this method works very successfully for most quantities, estimating electron density (and hence any quantity which includes mass) encounters problems when either the [SII] ratio or one of its error bars crosses the low density limit (corresponding to about 100 cm⁻³). Formally, the density could be anything below this limit. In

practice, however, the corresponding mass cannot be arbitrarily high, since at some point it fills all the available volume. Reversing this constraint, we use unit filling factor to set a robust lower limit to the density and therefore an upper limit to the mass. To define the volume one needs to adopt a depth behind each pixel, which we take to be 350 pc, or about 0'.5. In practice, these firm density limits are rarely much below the [SII] limit.

4. RESULTS: OVERVIEW

In Paper I our picture of the kpc-scale region of Mkn 78 was based mainly on a detailed morphological comparison of the radio and emission line regions, together with preliminary kinematic data from 10 FOS apertures. Here we introduce our new high resolution STIS $\lambda 5007$ spectra, and use them to develop the dynamical picture more fully, first heuristically (this section) and then quantitatively (§5). Fortunately, with one or two minor exceptions, our new results confirm and build on the scenario developed in Paper I.

In what follows, we divide the whole area into three regions (see Figure 1): (1) “W-knot”: the innermost western region, which includes the bright [OIII] feature and inner western radio ‘jet’; (2) “E-fan”: the bright eastern fan-like complex, with associated radio feature; and (3) “W-lobe”: the larger scale western region which includes several [OIII] components and a more extended radio ‘lobe’. We separate the regions in this way not just to help organize the discussion but, as discussed in Paper I, because they may also represent three stages in the development of a radio jet interacting with a denser cloud complex: (1) early stage before significant disruption; (2) later stage as cloud breakup and ablation ensue; (3) yet later stage when the cloud complex has been destroyed and dispersed.

4.1. Nucleus and Inner Western Region

As noted in Paper I, the radio jet emerges due west, bends to the WSW, and terminates in a weak lateral extension. In the vicinity of this radio feature lies the bright [OIII] LW–1 feature, suggesting a jet-gas interaction. However, our single FOS aperture (located just south of LW–1) indicated little disturbance, prompting our suggestion that the interaction was too recent to have seriously affected the cloud complex.

Our new STIS data help develop this picture somewhat. First, it is useful to clarify the near-nuclear [OIII] flux distribution by applying reddening corrections: is LW–1 a separate feature, or the outermost part of a larger region hidden by the dust lane? Panel 7 in Figs 3a and 3d shows the extinction rising across the dust lane ($A_V \sim 3^m - 5^m$) yielding a corrected [OIII] flux of high intensity interior to $\sim 0'.3$. Although the outer boundary of LW–1 is genuine, the inner boundary may not be — it appears in slit D but not in slit A. Given the uncertainties in the (large) reddening corrections we choose to downplay the independent existence of LW–1, and instead emphasize the close association of intense nuclear radio and [OIII] emission, with both terminating approximately together $\sim 0'.3 - 0'.5$ from the nucleus.

If there is [OIII] emission along the length of the radio jet, what is its kinematic state? Figure 4 shows this region in more detail for slits A and D. There is a clear drop in

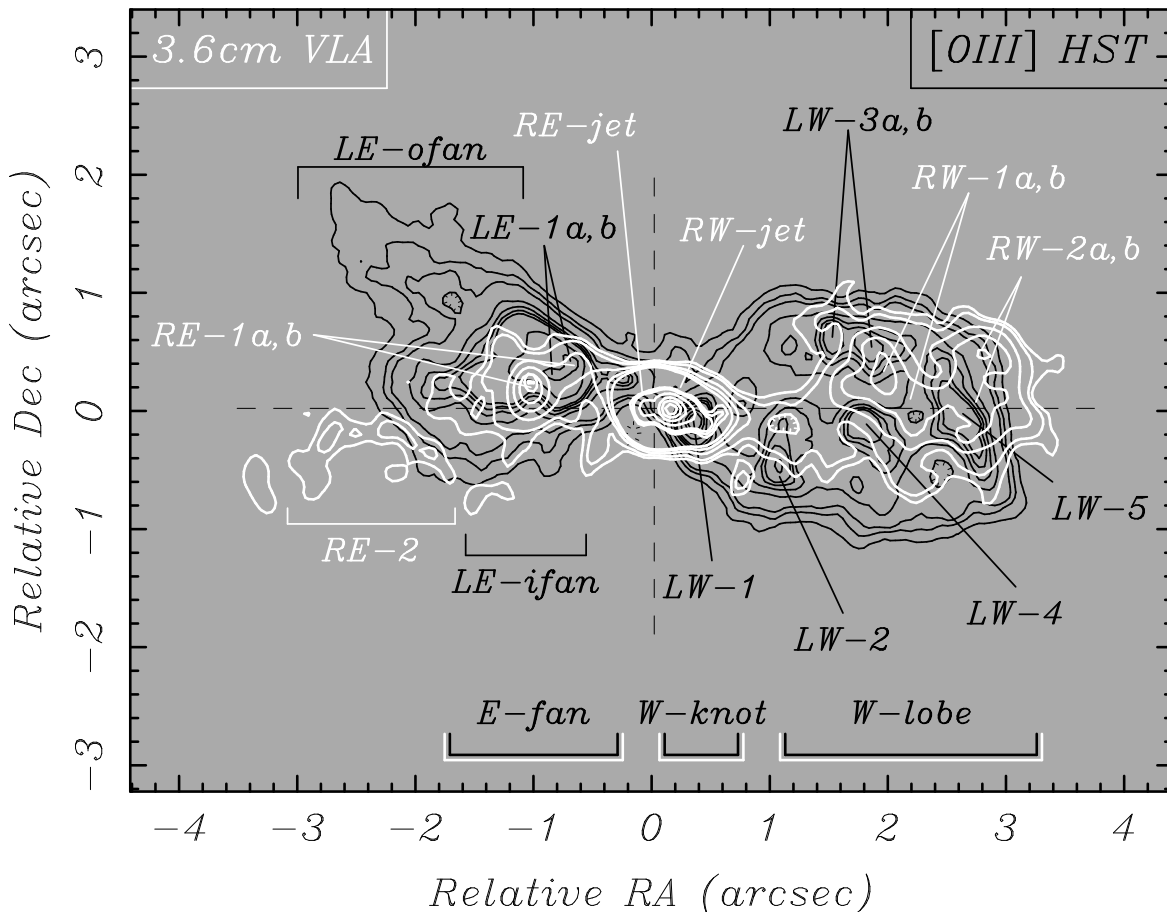


FIG. 1.— Contours of the $[OIII]\lambda 5007$ emission (black) and 3.6 cm radio emission (white), plotted to the same scale and registered. The radio map replaces the nuclear region with the core-subtracted uniform weight data. Major features are labelled, as well as the three principal regions which we study. See Paper I for more detailed versions of this figure.

linewidth and substructure moving away from the nucleus, becoming a single narrow ($\text{FWHM} \sim 300 \text{ km s}^{-1}$) profile towards the end of the jet near LW-1 (confirming our FOS measurement). More specifically, a 3-component Gaussian fit reveals red and blue components flanking a central component, with velocities dropping from $\pm 270 \text{ km s}^{-1}$ near the nucleus to $\pm 150 \text{ km s}^{-1}$ near the jet end (we ignore the narrow component adjacent to the nucleus in slit A since this is offset laterally from both the jet and the nucleus). This indicates a modest interaction over the brightest parts of the jet (behind the dust lane), becoming essentially undetectable at the jet end near where it bends.

Our basic conclusion in Paper I was of little “damage” to the LW-1 region compared to elsewhere in the NLR, despite morphological signs of a strong jet-gas interaction (the termination and flaring of the radio jet near LW-1). This conclusion still holds — there is evidence for some interaction between the radio jet and $[OIII]$ emitting gas, though the kinematic disturbance is modest and, at least where visible (i.e. at LW-1), there has been little dispersal of the line emitting gas. The clearest indication of the relative levels of disturbance near W-knot, E-fan and W-lobe is seen in Figure 2: the LW-1 spectral features in slits A and D are compact in both spatial and spectral dimensions, certainly compared to the broad multicomponent features seen elsewhere in the NLR. As argued in Paper I, this points to a young interaction in the W-knot

region — either the jet has only been active for a short time, or the gas has only entered its flow recently. We estimate the relevant interaction timescale in §5.1.

One final note concerns the true nucleus, which is visible in red images and is located in the middle of the dust lane, $0''.34$ East and $0''.13$ North of the peak of LW-1 (see Paper I §3.7). Slit D passes across the nucleus and reveals a relatively well defined emission feature spanning ~ 3 pix ($\text{FWHM} \sim 0''.13 \equiv 95 \text{ pc}$) with roughly symmetric velocity profile centered on systemic with $\text{FWHM} \sim 390 \text{ km s}^{-1}$ and flux $3.5 \times 10^{-15} \text{ erg cm}^{-2} \text{ s}^{-1}$ (dereddened by $A_V \sim 3.8^m$ to $1.15 \times 10^{-13} \text{ erg cm}^{-2} \text{ s}^{-1}$; see Figures 2, 3d and 4). We speculate that this is the “normal” NLR component, which might be present in the absence of the radio source. This is supported by the fact that the $[OIII]$ linewidth falls nicely on the “virial” correlations between $[OIII]$ FWHM and either bulge luminosity ($M_{B, \text{bulge}} \sim -20.8$, $H_o = 50 \text{ km s}^{-1} \text{ Mpc}^{-1}$ Whittle 1992a,b) or stellar velocity dispersion ($\text{FWHM}_{\text{stars}} = 406 \pm 40 \text{ km s}^{-1}$, Nelson & Whittle 1995, 1996). These relations apply for the majority of Seyferts which *don't* have relatively luminous linear radio sources. Of course, the integrated $[OIII]$ profile for Mkn 78 falls well off these relations since it has additional jet-related line broadening.

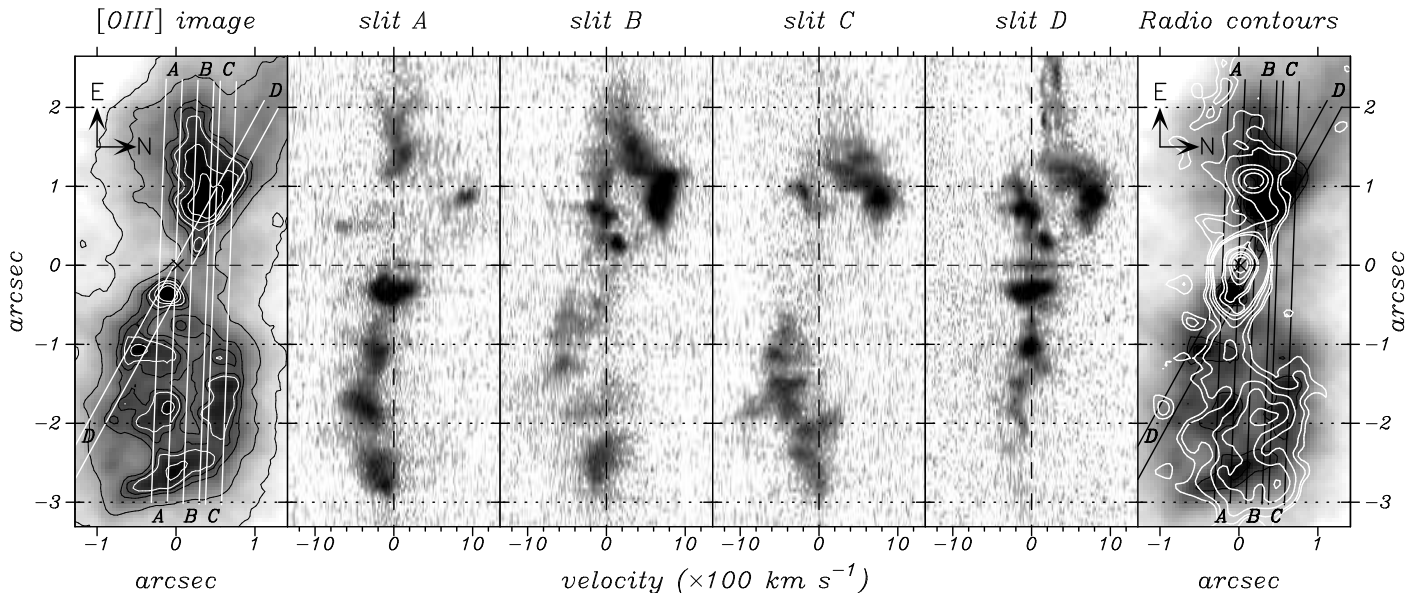


FIG. 2.— High dispersion (G430M) observations of the $[\text{OIII}]\lambda 5007$ emission line from the four slits. The position of the slits is shown overlaying the $[\text{OIII}]$ image (left) and the 3.6 cm radio image (right, with uniform weight data in the core region). The spatial axes of all datasets have been registered (including a compression for slit D), and the wavelength axis of the spectral data has been converted to velocity. All grey scales are logarithmic.

4.2. Eastern Fan

As discussed in Paper I, the eastern fan region provides perhaps the strongest morphological and kinematic evidence for a jet-gas interaction in Mkn 78: (a) the region has high surface brightness with upstream edge brightening and downstream flaring; (b) the radio source emerges ENE from the nucleus and is deflected by $\sim 45^\circ$ exactly at the head of the $[\text{OIII}]$ fan; (c) two ridges of emission start near the radio source and point away from the nucleus; and (d) ground based spectra (and our FOS aperture #9) show high velocities in this area.

Our STIS data reveal the velocity field across the region in much greater detail, and confirm the importance of jet-related kinematics. All four slits cross the eastern fan and show large amplitude ($\sim 800 - 1200 \text{ km s}^{-1}$) line splitting. The line splitting starts fairly abruptly $\sim 0''.4$ ($\sim 280 \text{ pc}$) from the nucleus, near the small $[\text{OIII}]$ feature LEm-a. The brightest of the two components is redshifted with approximately constant velocity ($700 - 800 \text{ km s}^{-1}$) spanning $\sim 0''.5 - 1''.0$ ($\sim 450 \text{ pc}$), while the weaker component is blue shifted, from ~ 0 to -300 km s^{-1} . Quite surprisingly, both these features are kinematically *narrow*, with FWHM only $\sim 200 \text{ km s}^{-1}$. Stated in physical terms, the gas acceleration mechanism is capable of generating flows with a turbulence to bulk ratio of as little as $\sim 20\%$.

The link to the radio source is fairly evident. Summarizing the morphological evidence from Paper I: the RE-1b component coincides with the two bright ends of the two ridges which flare back along the inner fan, while the stronger RE-1a component falls near an $[\text{OIII}]$ depression and begins the trend of radio emission along PA 120° . Thus, just where the $[\text{OIII}]$ is brightest, the radio source also brightens and bends through $\sim 45^\circ$. Turning to the kinematic evidence: the line splitting coincides, almost perfectly, with the RE-1 region, and as soon as these radio components leave the region the $[\text{OIII}]$ profiles

rapidly broaden (FWHM $\sim 400 - 600 \text{ km s}^{-1}$) and the bulk velocity drops, reaching low velocities after $\sim 0''.5$ (350 pc). This can be seen for slits B, C, D in Figure 2: the slits exit the radio source at $\sim 1''.0$, $\sim 1''.0$, and $\sim 1''.2$ respectively, each coinciding with the location in the spectral images of the transition between narrow redshifted emission and broader emission with decreasing velocity. In §5.5 we discuss two plausible contexts for this velocity pattern — gas exiting the jet flow experiences decelerating drag forces; gas further from the center of the interaction is accelerated less efficiently.

Returning to the overall velocity field of the eastern fan, if we include weaker features another pattern emerges: an elliptical-like shape is seen in the space-velocity images (see Figure 2, but identified more clearly in Figure 5 [still to be done]). Such shapes in this kind of observation usually indicate an expansion. Note that in this case, the central velocity is not at systemic, but at $\sim 200 \text{ km s}^{-1}$, suggesting that the expansion is occurring superposed on a bulk motion. There are two obvious possibilities for the origin of this bulk flow: it is part of the bipolar jet-driven velocity field; it is part of normal galactic rotation. Both seem plausible since the bipolar flow is certainly in this direction, while the eastern rotation amplitude is also close to 200 km s^{-1} (from Pedlar et al. 1989).

Overall, the evidence for jet-gas interactions in the eastern fan is strong. Furthermore, there is evidence for significant disruption of the gas: obviously the induced velocities are substantial, but also the gas is being dispersed and blown backwards, most likely by the radio flow since it seems to be deflected at this point. As argued in Paper I, here is an example of an interaction which has been going on for some time — at least long enough to accelerate the gas to high velocities and disperse some of it. This contrasts with the inner western region (discussed above) which seems much younger, or the outer western lobe which seems older and to which we now turn.

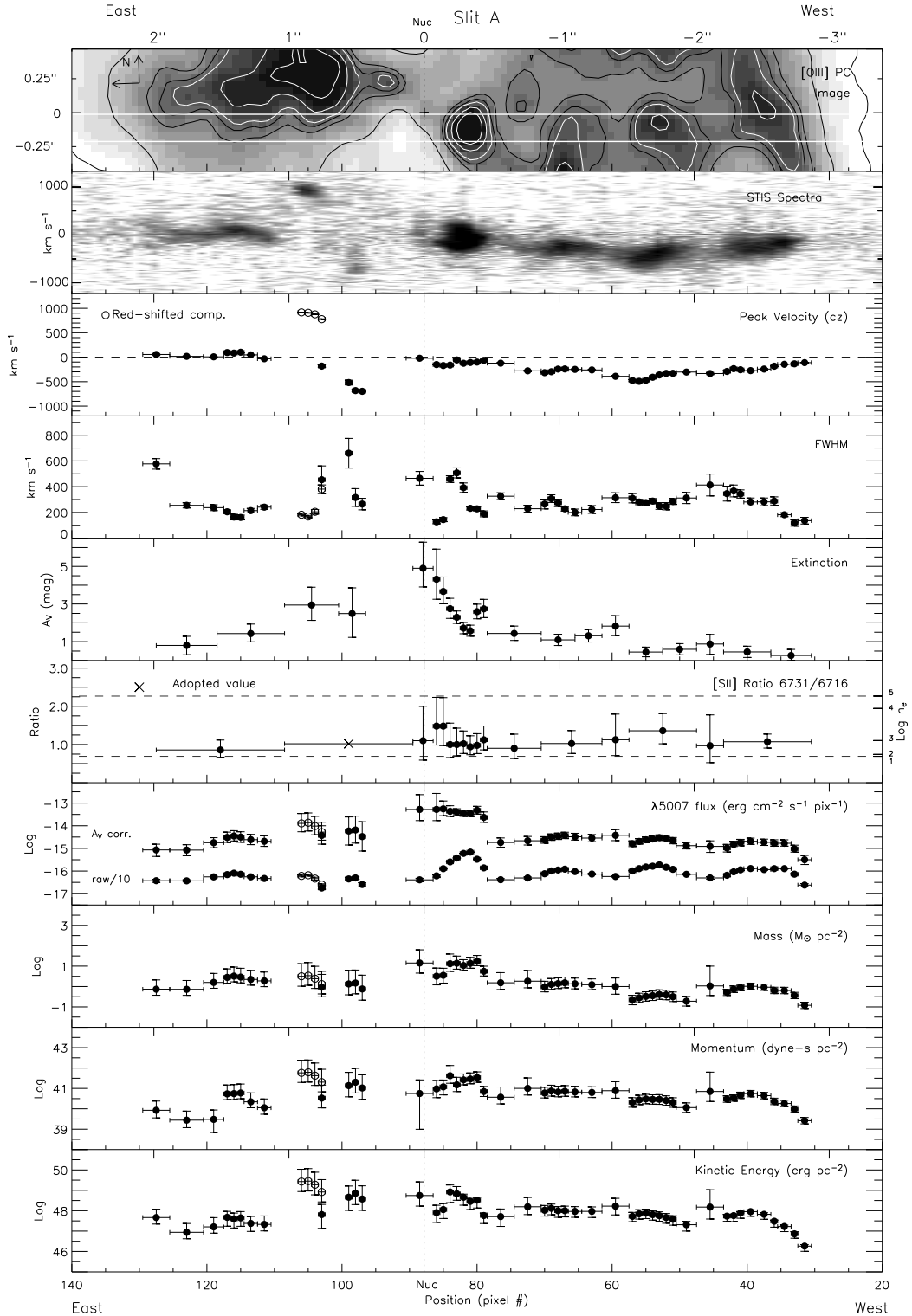


FIG. 3A.— Physical properties derived for the ionized gas along slit A. See text for details.

4.3. Outer Western Lobe

Beyond the inner W-knot region there are extended radio and [OIII] ‘lobes’, both comprising a number of individual features/knots spread over a diffuse background (see Figure 1). Slits A, B, and C cross much of this lobe, while slit D includes one of the [OIII] features (LW-2)

before exiting the region to the south.

First, it is important to establish the degree to which patchy obscuration has affected the appearance of the region, in particular whether any [OIII] ‘features’ are artifacts of absorption. In panel 7 of Figures 3a–d, one can compare the raw [OIII] flux distributions along each slit with the extinction corrected distributions. This suggests

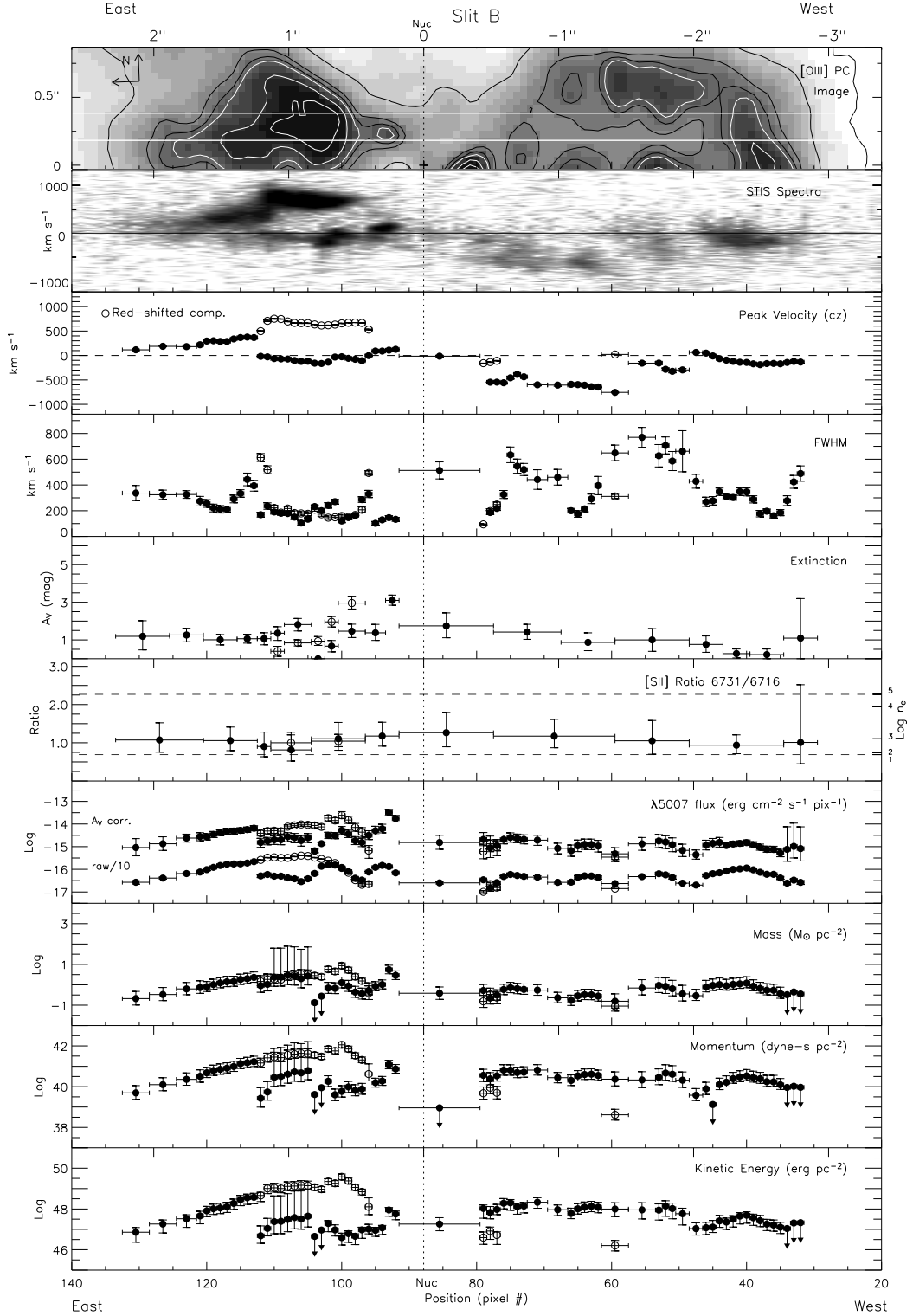


FIG. 3B.— Same as Figure 3a, for Slit B.

that some of the [OIII] features, though not all, may indeed be enhanced by extinction. In slit A, for example, the gap between LW-2 and LW-4 is probably caused by absorption, but the gaps between LW-1 and LW-2 and between LW-4 and LW-5 seem to be real. Similarly, the apparently faint channel along which slit B passes is created at least in part by dust: the extinction corrected

fluxes towards the nucleus are in fact similar to the values in the LW-5 feature at the western end, though they are still weaker than the LW-3 feature in slit C to the north. We conclude that while the exact distribution of ionized gas may be confused by patchy dust, inhomogeneities still seem to be present.

Turning to the velocity field, we note several general

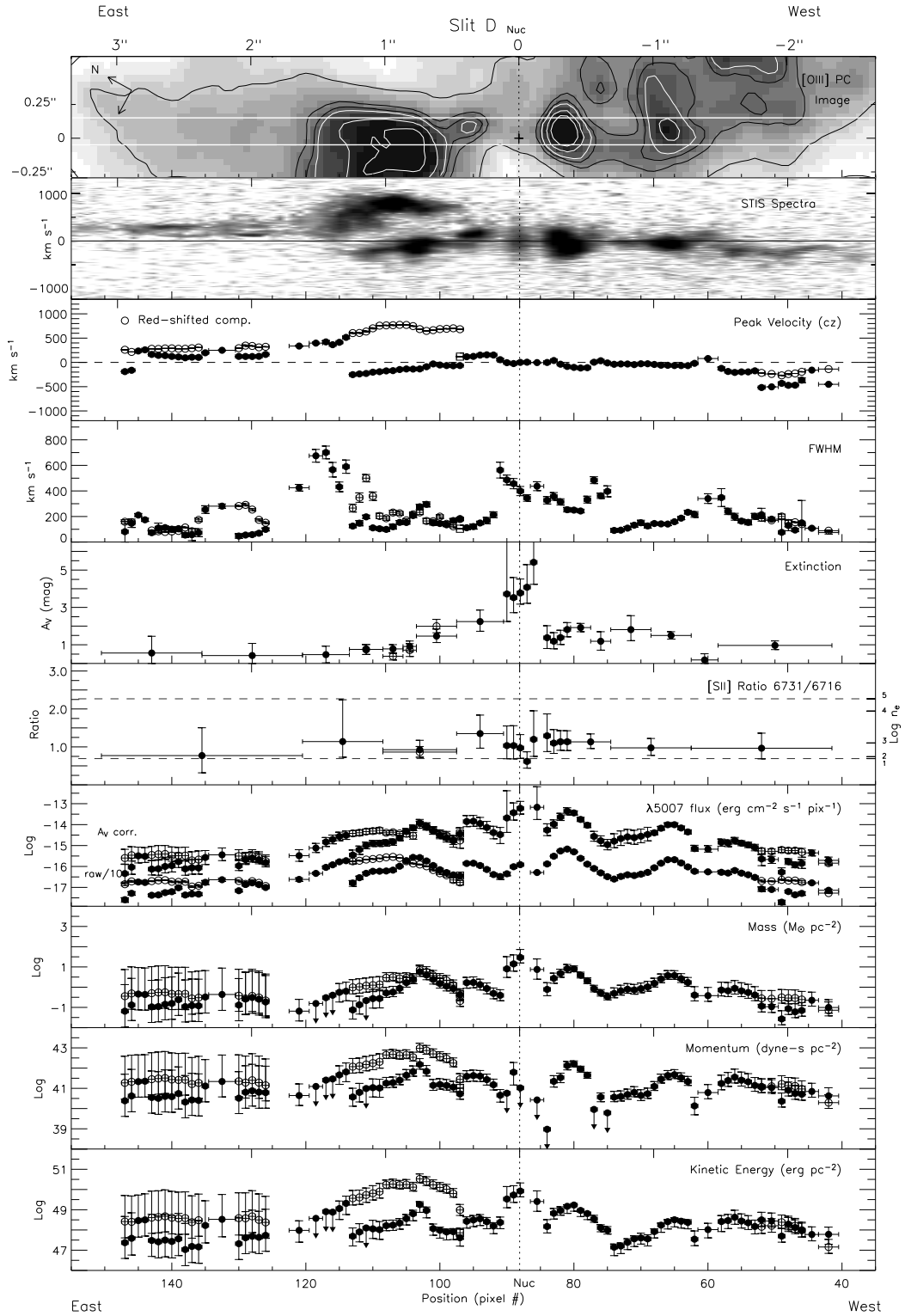


FIG. 3D.— Same as Figure 3a, for Slit D.

high amplitude disordered velocity field superposed on a basic bipolar outflow. This is consistent with our suggestion that the radio source interaction in W-lobe is older than at either W-knot or E-fan. The interaction has thoroughly broken up a pre-existing cloud complex and is currently dispersing it. This may also explain the absence of a simple shell-like geometry, with radio source surrounded

by [OIII] emission. Rather, the expanding [OIII] gas is breaking up, with radio emitting material flowing between and through the knots, extending beyond the [OIII] emission. The metaphor from Paper I still seems applicable: a dispersing cloud system comprising a leaky bubble.

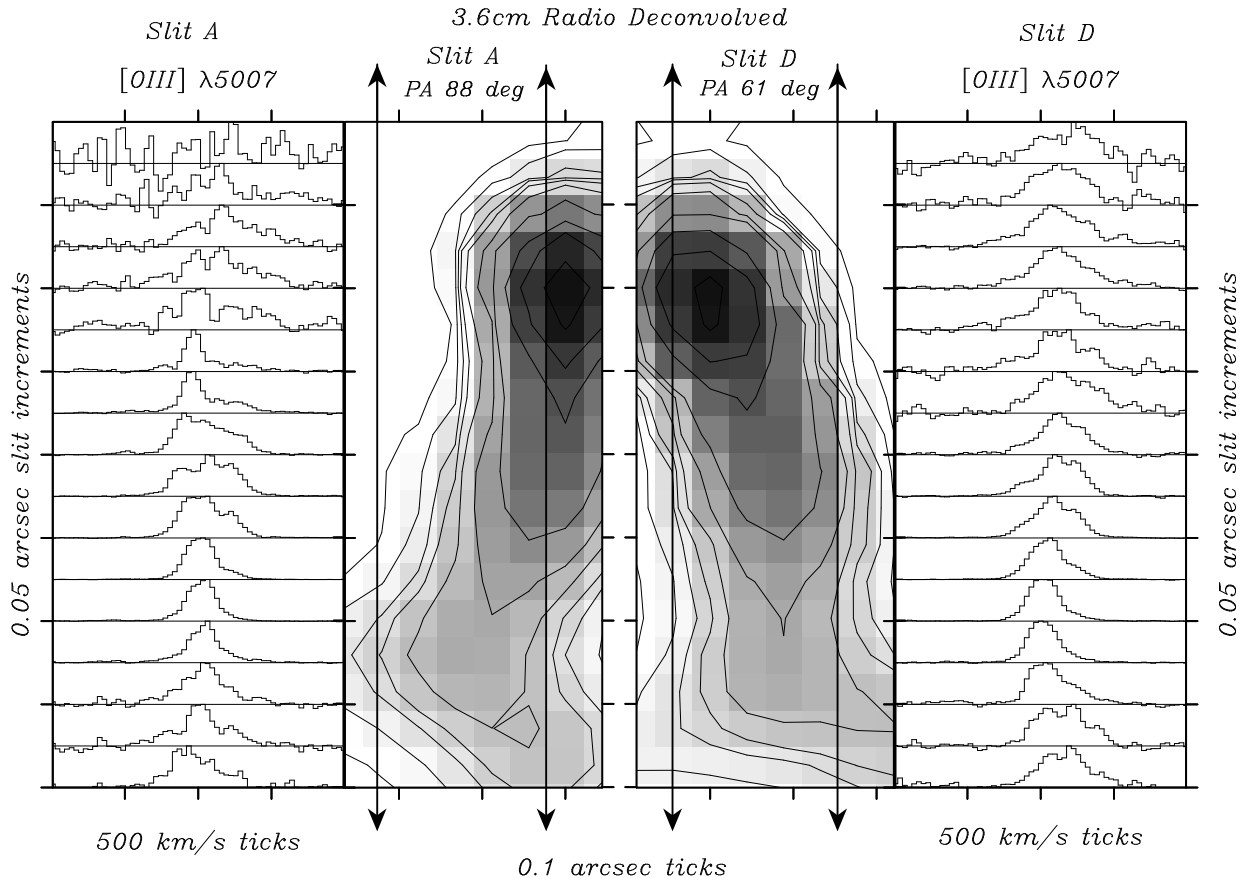


FIG. 4.— Detailed view of the inner western jet region (W-knot). The inner two panels show slits A and D superposed on a grey scale and contour plot of the deconvolved 3.6cm uniform weight *radio* map. The peak coincides with the true nucleus which lies behind the dust lane and is included only in slit D. On either side are shown the corresponding autoscaled [OIII] λ 5007 profiles. The slits coincide near the bottom of the figure over LW-1 (inc. # 80; yielding identical [OIII] profiles). See text for discussion of the profile shapes.

5. REGION PROPERTIES

In this section we develop a more quantitative analysis of the three major regions, W-knot, E-fan, and W-lobe, aiming to derive their basic physical properties and establish the most likely modes of interplay between the various components. While this is an important goal, our real interest is in using these properties to infer the nature of the jet flow, which we do in the following section.

Broadly speaking, we are concerned with four components: emission line gas; relativistic magnetoionic gas; the ambient ISM; and a jet which may contain thermal as well as relativistic gas. For each component, we are interested in energies, momenta, pressures and timescales. In what follows we will need a number of simple relations to evaluate these quantities, and rather than include all the details directly in the text we prefer to gather the necessary relations, together with their assumptions and symbol definitions, into Appendix A, which should be consulted as necessary. Note that in the Appendix, we group the relations by component: the emission line gas; the relativistic gas; the ambient ISM; and the jet.

Table 1 gives all *observed* quantities, taken either from Tables 3 and 4 in Paper I or measured directly from the data, while Table 2 gives *derived* quantities, taken either directly from Figures 3a – d or evaluated using the measured quantities given in Table 1 and the relations given in Appendix A. In cases where we use values taken from

Figure 3, we apply a simple correction factor based on the flux weighted area covered by the slits: 100%/80%/70% respectively, for W-knot/E-fan/W-lobe. This last sentence illustrates a convention we shall adopt: quantities evaluated for the three regions W-knot, E-fan, W-lobe may be given as, for example, Q1/Q2/Q3.

5.1. Timescales

Estimating the duration of the jet-gas interactions is important, not least since it allows interconversion of energies to luminosities, and momenta to forces. Given the apparent progression from compact to diffuse regions, we use crossing times to estimate ages. With length-scales \sim kpc and velocities $\sim 10^3$ km s $^{-1}$, clearly crossing times are \sim Myr. Table 2 gives more specific values, with $\sim 0.4/4.0/8.2$ Myr for the three regions respectively, and we indeed find the age progression expected.

These values need some explanation. First, since velocities are not constant across regions we prefer not to use Equation A15, but instead integrate the crossing time along the radial direction:

$$t_{cross} \sim \int_{r_o}^{r_o+D} dr/V = \frac{D}{V_1 - V_2} \ln \left(\frac{V_1}{V_2} \right) \quad (1)$$

where t_{cross} is the time to cross distance D starting at V_1 and ending at V_2 , assuming constant acceleration. For E-

fan we take: $400 - 400 - 100 \text{ km s}^{-1}$ across $0 - 0''.8 - 1''.6$, and for W-lobe we take $100 - 400 - 100 \text{ km s}^{-1}$ across $0 - 1''.25 - 2''.5$. Second, the choice of 400 km s^{-1} for E-fan represents the median of the red and blue shifted components, since this is likely to be the outward velocity component, the line splitting resulting from the superposition of outflow and lateral expansion. Third, the compact W-knot is more problematic since it has almost no translational velocity. Instead, we assume its size results from spreading due to internal velocities. We take the radius of the knot (measured parallel to the dust lane, $\simeq \frac{1}{2} \times 0''.25$) and half the velocity difference between the red and blue components of the [OIII] profile ($\simeq 200 \text{ km s}^{-1}$).

Finally, these timescales (and other quantities) depend on region geometry through projection factors. The simplest assumption is radial outflow at angle ϕ to the plane of the sky. Thus radial velocities and distances suffer projection factors of $\sin \phi$ and $\cos \phi$ respectively, and hence our age estimates also include a $\tan \phi$ factor. For present purposes, the uncertainty introduced by these projection factors ($\lesssim 2$) can be readily absorbed in the approximate nature of the estimates.

There are two other timescales worth noting, both radiative loss timescales. Anticipating results from §5.3, the energy stored in the radio source, E_{rel} , is lost through synchrotron emission on a timescale $E_{rel}/L_{rad} \sim 2 - 6 \times t_{age}$. Hence, radiative losses to the relativistic component, while present, don't dominate. Similarly, the thermal and ionization energy, E_{th} , stored in the line emitting gas is lost due to line emission on a timescale $E_{th}/L_{em} \sim 10^{-5} - 10^{-6} t_{age}$. Not surprisingly, the emission line region must be continuously reheated and reionized.

5.2. Mass & Distribution of Ionized Gas

Estimating ionized gas masses is relatively straightforward, complicated in our case only by uncertainties in reddening and gas density. We have adopted values directly from Figure 3, corrected only for area missed by the slits. These values agree roughly with simpler estimates using Equation A1 and average region properties given in Table 1. Since $L_{H\beta}$ and n_{em} are similar in all three regions, the ionized gas masses are also similar: $0.4/1.1/1.3 \times 10^6 M_{\odot}$. We have little handle on neutral gas which probably dominates over the ionized gas. However, if the acceleration and ionization processes are related (directly or indirectly) then it is the ionized gas which constrains the physics of the acceleration process, not the neutral gas.

Although the three regions have quite different sizes, they do in fact subtend roughly the same solid angle at the nucleus: $\Omega/4\pi \sim 5\%/5\%/10\%$. Perhaps not surprisingly, using Equation A2 we find the ionized gas filling factors are all low and decrease with increasing region size: $\log ff_{em} \sim -2.2/-3.8/-4.3$. As with all AGN emission regions, therefore, it seems the ionized gas in these disturbed regions occupies only a small fraction of the total volume and comprises only a small fraction of the total (dynamical) mass.

Critical to emission region properties is, of course, the nuclear ionizing radiation. Although this is heavily obscured, we can use the FIR luminosity $L_{IR} \approx 1.3 \times 10^{44} \text{ erg s}^{-1}$ as surrogate since ultimately most of the UV and line radiation is absorbed and reradiated by dust in the

$60 - 100 \mu\text{m}$ band (see Paper II §8.2, and Equation A8). Using the inferred UV luminosity we estimate the radiation parameter and Stromgren depth for the ionized gas (Equations A10 and A11): $\log U_{em} \sim -2.2/-2.8/-3.3$, $\log N_{em} \sim 20.9/20.3/19.8 \text{ cm}^{-2}$ (adopting $n_{em} = 10^3 \text{ cm}^{-3}$ throughout). These values, including the gradient in radiation parameter are quite similar to the direct estimates from line ratios given in Paper II.

Pushing slightly further, the cloud column and gas densities give a rough estimate for cloud sizes, allowing us to convert filling factors to local covering factors using Equation A3, yielding $cf_{em} \sim 0.6/0.5/0.6$. From the nuclear perspective, therefore, the regions are fairly well blocked, not only to the ionizing radiation but also any radially moving jet flow. Finally, the local covering factors and region solid angles together yield an intercepted UV luminosity: $\log L_{UV,int} \sim 42.7/42.7/43.1 \text{ erg s}^{-1}$. The surprisingly good agreement between these values and our *measured* emission line luminosities ($L_{em} \equiv 10 \times L_{5007}$, from Equation A14): $\log L_{em} \sim 42.8/43.2/43.3 \text{ erg s}^{-1}$, lends strong support to our use of the FIR emission as surrogate for the UV luminosity and, of course, the overall importance of nuclear source photoionization (Paper II §8).

While the agreement between our simple analysis and several measured quantities is gratifying, we should never expect detailed agreement — obviously the estimates are idealized approximations, but also, as shown in Paper II, the most likely form for the ionized gas is a *range* of optical depths, with both optically thick and thin components.

5.3. Energies and Luminosities

Across the regions, energy resides in various components. The ionized gas carries kinetic and thermal energy while the relativistic component carries energy stored in the magnetic fields and particles. The regions expand and do work on the surrounding ISM, releasing energy which may find its way into both ionized and relativistic components. Energy is brought into the regions through the jet flow and nuclear UV radiation, while energy leaves the system through line and synchrotron radiation as well as adiabatic losses. Some of these we measure as total energies, while others we measure as rates, or luminosities. Using our estimated ages, however, we can convert between the two.

First some details: (1) There is ambiguity over which radio components to associate with the two inner regions. For W-knot, it is likely that both the inner and outer western radio jet interact with the [OIII] feature at LW-1. Likewise, it is likely that both RE-jet and RE-1 interact with LE-ifan. We therefore quote values for both radio components in Table 2 and, when necessary, take their sum. (2) We distinguish between the energy of the relativistic component E_{rel} (Equation A22) and the total energy of the region, E_{lobe} (Equation A26), which we assume includes a thermal component in pressure balance with the relativistic component. Their relative dominance is determined by ff_{rl} , the filling factor of the relativistic component. Although in this section we use E_{rel} (making the usual choice of $ff_{rl} = 1$), in other circumstances we prefer E_{lobe} , partly because it is less sensitive to ff_{rl} (see Equation A26) but also because it more closely tracks the total stored energy

(note that for a wide range of ff_{rl} , $E_{lobe} \approx E_{rel,ff=1}$). (3) When considering the work done as the regions expand into the ISM (L_{exp} , Equation A29), we make two assumptions. One is that the relativistic pressure in the lobe is balanced by the ram pressure of the lobe expansion. The other concerns the lobe expansion velocity. Although the natural choice is the [OIII] velocity, this could be a lower limit if the expansion is dominated by a jet which flows around the ionized gas at higher speeds. With local covering factors $cf_{em} \sim 50\%$ (see previous section) the jet is unlikely to percolate efficiently. We take the conservative assumption that the region, as defined by the [OIII] emission, expands at the [OIII] velocity.

From Table 2 we can rank the various energies in decreasing order of importance: E_{ph} ; E_{em} ; E_{ke} ; E_{rel} ; E_{exp} ; E_{rad} ; E_{th} (using, in order, Equations A8, A14, A5 and A6, A22, A29, A19, and A7, where we have converted L_{ph} , L_{em} , L_{rad} , L_{exp} to their corresponding energies using the region ages). Roughly speaking, these divide into three groups, with relative values ~ 1000 ; 1000 ; 1 ; 1 ; 1 ; 0.3 ; 0.01 .

Our first major conclusion, therefore, is that *photon energy* dominates by a factor of 1000 over all others, in particular the kinetic and relativistic energies. Furthermore, the emission line luminosity is roughly equal to the incoming UV radiation (in this case inferred from the FIR emission). Both these facts support the conclusions of our emission line study in Paper II, which identified photoionization as dominant, particularly when compared to shock ionization.

Turning to consider the origin of the kinetic energy in the ionized gas, we note that it is comparable (to factors $\lesssim 2$) to the energy stored in the relativistic component or, equivalently, the shock energy liberated by the expanding lobe over the lifetime of the region (i.e. $L_{exp} \times t_{age}$). This similarity, independently true for each region, provides strong evidence that the flows driving the region expansion and its associated radio source, also accelerate the ionized gas.

The kinetic energy of the ionized gas is also significantly greater than its thermal energy: $E_{ke} \sim 200E_{th}$ ($\sim 80E_{th}$ if ionization energy is included). This follows directly from the fact that 10^4 K is much cooler than gas behind a shock with the [OIII] velocity V_{em} . Either the ionized gas has not experienced such shocks or, if it has, it has cooled considerably from post shock temperatures $\sim 4 \times 10^5 V_{sh,2}^2$ K (where $V_{sh,2}$ is a shock velocity in units of 10^2 km s $^{-1}$). The ubiquity of shocks is, of course, highly likely since typical velocities are so much higher than the sound speed of a 10^4 K gas (~ 10 km s $^{-1}$). This places an important demand on the overall acceleration process: it must allow efficient post shock cooling.

Turning to consider the energy stored in relativistic component: despite decreasing lobe pressures ($P_{rel,-10} \sim 9/0.5/0.2$ where P_{-10} signifies units of 10^{-10} dyne cm $^{-2}$), the increase in volume more than compensates and the total energy in relativistic particles and fields increases for the three regions: $\log E_{rel} \sim 53.2/53.7/54.4$ erg (taking $ff_{rl} = 1$ in Equation A22). This is, naively, what one expects given their increasing ages (recalling that synchrotron losses don't dominate). Indeed, allowing for region age reveals an approximately constant energy input

to the relativistic component: $\log L_{rel} \equiv \log(E_{rel}/t_{age}) \sim 40.1/39.7/40.0$ erg s $^{-1}$. If this energy input ultimately comes from the nuclear jet and is the main repository of the jet energy (which we discuss in more detail in §6.2), then the result is consistent with an approximately constant jet power of $\sim 10^{40}$ erg s $^{-1}$ over the total lifetime of the visible regions, ~ 10 Myr.

Of course, relativistic components are thought to originate via shock related particle reacceleration. Could the relativistic component arise from shocks associated with lobe expansion? Unfortunately, although we find good quantitative agreement between L_{rel} and L_{exp} , this provides no real insight since, as evaluated here, both luminosities depend on the product: $P_{rel}A_{lobe}V_{em}$. An alternative approach is to compare L_{exp} with L_{rad} , the radio luminosity — can the shock luminosity at least power the radio luminosity? In this case, we find that it can, with $L_{exp}/L_{rad} \sim 5/8/5$ for the three regions. While the conditions may be somewhat different, this ratio is similar to the efficiencies with which supernova remnants transform shock energy into relativistic particles, $\sim 20\%$ (e.g. Blandford & Eichler 1987). Perhaps the value of this comparison is to support the credibility of evaluating L_{exp} — namely that the regions expand with roughly the [OIII] velocity, such that the external ram pressure balances the internal relativistic pressure.

5.4. Momenta and Forces

An alternative approach is to focus on momentum rather than energy, making use of the identities: force = momentum/timescale = pressure \times area. The central aim is to identify what provides the ionized gas with its momentum, G_{em} , or equivalently which force provides its momentum flux, $\Pi_{em} = G_{em}/t_{age}$. The two obvious candidates to consider first are the pressure found in the relativistic gas (Equation A21), and the radiation pressure (Equation A12). From Table 2, we see that both are marginal possibilities. The relativistic pressure acting over the region dimensions gives $\Pi_{rel} \approx P_{rel}A_{lobe}$ whose values for the three regions are $\sim 40\%/20\%/80\% \times \Pi_{em}$, while the radiation pressures acting over about half that area (because the covering factor is $\sim 50\%$) gives $\sim 30\%/15\%/50\% \times \Pi_{em}$. It is not entirely clear how to regard these values. While they seem to be systematically below the required values by about half a dex, perhaps within the considerable uncertainties they should be considered as a reasonable match.

There are two other considerations, however, which shed light on possible acceleration mechanisms. First, we have independent estimates of the column density in the ionized gas. Can either P_{rel} or P_{rad} accelerate these columns adequately? Equation A18 gives the relation between pressure, column, and acceleration, and if we evaluate this we find the maximum columns are $\sim 1 - 2 \times 10^{20}$ cm $^{-2}$ for both P_{rel} and P_{rad} . Once again, these are plausible though somewhat less than the preferred columns indicated by the photoionization models explored in Paper II, which suggest $N_{em} \sim 10^{21} - 10^{22}$ cm $^{-2}$, at least for the optically thick component. Second, there are simple geometrical considerations. For example, radiation pressure acts in a purely radial direction, and hence it cannot easily explain any significant lateral bulk motion. If the pres-

ence of split lines indeed indicates lateral motion, which seems most likely, then this would argue against radiation pressure as the dominant accelerating force. Conversely, a simple overpressure in a given region would not obviously generate a strong bipolar flow, but rather a general expansion with associated broad and/or split lines centered about systemic velocity.

Combining these perspectives, it seems that neither pure P_{rel} nor pure P_{rad} forces are ideal candidates for accelerating the ionized gas. While they may indeed play some role in some circumstances, it seems there is a need for a stronger driving force with the potential for both radial and lateral acceleration. The obvious candidate is a jet flow, whose *dynamical* (ram) pressure is higher than either P_{rel} or P_{rad} . As we discuss further in §6.4, there is good evidence that the jet flow does indeed have a ram pressure somewhat higher than its internal pressure.

5.5. Pressures and Confinement

Although we have assumed the radio lobes are in a state of expansion, it is worth checking how the various pressures compare throughout the system, and in particular whether static or dynamic pressure balance is occurring.

First, note that although Mkn 78 is a typical radio quiet Seyfert, its radio source pressures ($P_{rel,-10} \sim 0.2 - 10$) are at least as high if not higher than the hot spots in classical radio galaxies ($P_{rel,-10} \sim 0.04$, e.g. Miley, 1980; note from Equation A20 that since the equipartition field depends on synchrotron volume emissivity, then the small size of Seyfert radio lobes compensates for their relatively low surface brightness). These high pressures, together with their radial decrease, almost certainly reflect their location in the high pressure environment of a near nuclear galaxy ISM. Estimating the pressure in this ambient medium is, however, quite difficult especially in the absence of good X-ray imaging. Taking canonical values, $n_{ism} \sim 1 \text{ cm}^{-3}$ and $T_{ism} \sim 10^6 \text{ K}$ gives thermal pressures, $P_{th,-10} \sim 1.4$, comparable to P_{rel} confirming that the radio source could be in rough pressure equilibrium with the ambient ISM. Could the expanding radio source be in *dynamical* pressure equilibrium with the ambient medium? Equation A30 gives the ISM density, n_{ism} , which allows a radio lobe pressure P_{rel} to drive forward into the ISM at velocity V_{lobe} in ram pressure balance. If we take $V_{lobe} \approx V_{em} \sim 50/100/100 \text{ km s}^{-1}$ at the front of the lobe, then we find $n_{ism} \sim 10/0.2/0.1 \text{ cm}^{-3}$. Within the (considerable) uncertainties, these are plausible ISM densities, confirming the possibility that the lobe expansion could indeed be constrained by ram pressure. Thus, it seems the radio sources in Mkn 78 are intimately constrained by the ambient ISM: their overall pressures are probably set by being located in the ISM, and their front boundaries experience transonic expansion. Note that at $T_{ism} \sim 10^6 \text{ K}$ the sound speed is $c_{ism} \sim 100 \text{ km s}^{-1} \sim V_{lobe}$, consistent with our previous statement. Note also that the condition of dynamical pressure balance would not hold for expansion speeds similar to the maximum (center lobe) velocities $V_{em} \sim 400 \text{ km s}^{-1}$ which require significantly greater pressure to drive them. This is perhaps as one might expect since motion wholly within the radio source does not interface directly with the external ISM.

A similar approach to testing the basic picture of lobe

development is to invoke the model of Begelman (1996) and Bicknell, Dopita, & O’Dea (1997) which describes how a jet inflates a lobe as it burrows into an ISM with decreasing density $n_{ism} \propto r^{-\delta}$ (Equations A31 – 33). Taking values of lobe size, pressure and age from Tables 1 and 2, and adopting density gradients $\delta = 0, 1, 2$, we find ISM densities $n_o \sim 0.1 - 0.5 \text{ cm}^{-3}$ at $\sim 1 \text{ kpc}$; lobe expansion speeds $V_e \sim 100 - 200 \text{ km s}^{-1}$; and jet luminosities $L_j \sim 0.7 - 1.5 \times 10^{41} \text{ erg s}^{-1}$. For our current purposes, the most important of these is the ISM density, which is close to (perhaps a little under) the canonical value of $\sim 1 \text{ cm}^{-3}$ for the low density ISM phase. The values for lobe expansion speed and jet luminosity, while gratifyingly close to our expectations, are really only testing basic consistency since they are already loosely tied to our input values for lobe age ($V_e \sim x_e/t_{age}$) and lobe pressure ($L_j \sim E_{lobe}/t_{age} \sim P_{lobe}x_e^3/t_{age}$, see §6.2). Nevertheless, it is important that both the rough analysis (previous paragraph) and a more detailed model (this paragraph), both show consistent and plausible values for jet, lobe, and ISM properties under the basic scenario of a jet inflating a lobe which expands into the ISM driven by its internal pressure.

Turning to another important phase: how does the pressure in the *ionized gas* compare to that in the surrounding radio source? The approximate equivalence of radio source pressures and ionized gas in Seyferts has long been known (e.g. de Bruyn & Wilson 1978). Can we confirm this in detail for Mkn 78? The most straightforward analysis takes at face value the density and temperature estimates from the [SII] and [OIII] emission lines, finding similar pressures throughout: $P_{em,-10} \approx 16$ ($n_{em} \sim 10^3 \text{ cm}^{-3}$, $T_{em} \sim 1.2 \times 10^4 \text{ K}$, Equation A13). These are somewhat higher than the pressures in the radio sources, which drop with radius, from $P_{rel,-10} \sim 4 - 14$ near RW–jet, to $\sim 0.2 - 0.5$ in RW–lobe. There are, however, at least two reasons to be cautious about the [SII] density estimates. First, the [SII] ratio error bars can approach or even cross the low density limit, particularly at larger radii where the emission is weaker, allowing values lower by $\sim 1 - 2$ decades. Second, the [SII] lines may be dominated by emission from denser than average regions, a possibility made more likely by our finding in Paper II that the ionized gas comprises a mixture of optically thick and thin components.

An alternative approach to probing ionized gas pressures is to use the ionization parameter, U_{em} , which can be expressed either as a ratio of photon to gas densities or, equivalently, photon to gas pressures. From Paper II we find $U_{em} \propto r^{-1}$, decreasing from $\sim 10^{-2}$ near W–knot to $\sim 10^{-3}$ at the outer edge of W–lobe. Since ionizing flux falls as r^{-2} , we therefore expect $n_{em} \propto r^{-1}$ and hence $P_{em} \propto r^{-1}$, which more closely matches the gradient in P_{rel} . Quantitatively, Equations A9 and A10 combine (using $\alpha_o = 1.4$, $\lambda_{low} = 4000 \text{ \AA}$, $T_{em} = 12000 \text{ K}$) to give $U_{em} \approx 0.012 P_{rad}/P_{em}$. Taking P_{rad} and U_{em} from Table 2, we find $P_{em,-10} \approx 4$ near LW–1, becoming ≈ 1 in the center of W–lobe and ≈ 0.4 at the outer edge of W–lobe. These values now match P_{rel} fairly well, certainly within the considerable uncertainties of the method. With these revised density estimates, therefore, it seems that the relativistic and line emitting components could be in rough pressure balance throughout the regions.

Summarizing this section, we have begun to construct

a detailed picture of the emission region properties: (a) we confirm an age sequence for the three regions, ranging from ~ 0.4 to 8 Myr for W-knot to W-lobe; (b) we find the regions contain $\sim 10^6 M_\odot$ of photoionized gas with significant covering factor but low filling factor; (c) the region's energy throughput is dominated by photons, with kinetic and relativistic energies a distant second; (d) the rough equivalence of the kinetic, relativistic, and mechanical energies confirms that acceleration of the ionized gas is related to the expanding radio source; (e) however, it is doubtful whether either internal lobe pressure or radiation pressure can themselves accelerate the ionized gas; (f) it does seem likely, however, that the internal lobe pressure can drive the lobe expansion into the ISM at speeds comparable to that of the ionized gas at the front of the lobe; (g) the relativistic and ionized components seem to be in rough pressure balance throughout the regions.

While these conclusions give useful insights into the nature of the emission regions, we are still missing a crucial component in the overall system: the jet flow. One of the main reasons for evaluating the region properties is to use these properties to infer properties of the jet flow. This is the topic to which we now turn.

6. JET PROPERTIES

In this section we try to ascertain the properties of the underlying nuclear bipolar outflow — the jet. Since we only have limited observational access to the jet itself, we must use indirect constraints provided by its interaction with the other components, in particular the ionized gas. Two of the most important jet properties are its total momentum flux and its luminosity which, we argue, can be estimated via simple conservation conditions together with a number of correction factors, α . Having obtained values for the bulk jet properties, we refine our knowledge of the jet by assuming it contains *two* components in approximate pressure balance: (a) a relativistic component of filling factor ff_{rj} , and (b) a non-relativistic, or thermal, component which is in approximate pressure balance with the relativistic component. General expressions for jet properties are given in Equations A34–A37, and for a two component jet in Equations A38–A41. Since it is unlikely that the jet has relativistic bulk motion on the length scales we observe, we may safely use the non-relativistic versions of these Equations.

6.1. Jet Momentum Flux

Since a purely relativistic gas has very low inertia, the fact that Seyfert jets clearly accelerate significant quantities of ionized gas indicates that they must contain an additional, thermal component, at least on the kpc scale.

What is the momentum flux of the Mkn 78 jet? To first order we have $\Pi_j \sim \Pi_{em} \equiv G_{em}/t_{age}$. This may be an underestimate for at least two reasons. First, not all jet material may be intercepted by the ionized gas, giving a correction factor related to the local covering factor: $\alpha_{cf} \simeq 1/cf_{em} \sim 2$, where cf_{em} is evaluated using Equation A3. Second, if drag forces act on the ionized gas then momentum is lost overcoming these forces. A simple estimate of these compares the column of intercloud material across the region with the column across a typical line emitting

cloud, N_{em} :

$$\begin{aligned} \alpha_{drag} &\sim 1 + \frac{n_{icm}D}{N_{em}} \\ &\approx 1 + 0.0015 N_{em,22}^{-1} n_{icm} \theta_x (cz/H_o) \quad (2) \\ &\approx 1 + 0.22 N_{em,22}^{-1} n_{icm} \theta_x \text{ for Mkn78} \end{aligned}$$

Photoionization models (see Paper II) suggest the ionized gas has $N_{em} \sim 10^{22}$, while dynamical arguments give similar values (see below). So, for the region sizes in Mkn 78 ($\theta_x \sim 0''.3/1''.2/2''.7$) we have α_{drag} in the range $1 - 2$, though it could be larger for optically thin gas of smaller column. There may be a third factor if the jet also accelerates the intercloud medium which itself has significant mass. However, to first approximation we consider this to be included in the first two factors, since to some extent it is the gas which percolates the ionized gas which would be accelerating the intercloud medium, and the drag forces may also be part of the process of accelerating this other material.

Combining these, we have $\Pi_j \simeq \alpha_{drag}\alpha_{cf}\Pi_{em} \simeq 2 - 5 \times \Pi_{em}$, where the lower value applies for no drag. For the three regions in Mkn 78 we have (see Table 2): $\log \Pi_{em} \simeq (32.8/33.1/32.9)$ dyne, suggesting a jet momentum flux of $\sim 2 - 5 \times 10^{33}$ dyne.

From Equation A38, we see that the jet momentum derives from a combination of the inertia of the thermal component (density n_{th}) and the inertia of the rest mass and energy in the relativistic component, with the first of these hugely dominant. The only possible way for a purely relativistic component (i.e. $n_{th} = 0$ and/or $ff_{rj} = 1$) to provide this momentum would be to have $V_{j,3}^2 P_{rel,-10} \gtrsim 10^7$ requiring $V_j \approx c$ and P_{rel} above its equipartition value by a factor $\sim 10^2 - 10^3$. Alternatively, anticipating results in §6.2 and §6.3, note that a purely relativistic component has (see the end of Appendix A): $c\Pi_j/L_j \approx \beta_j$, where $\beta = V_j/c$. Since our estimates of $c\Pi_j/L_j$ are $\sim 200 - 2000$ this is clearly unphysical (unless our estimates of jet energy flux are too low by factors $10^3 - 10^4$, which seems unlikely).

In contrast, a modest thermal component and jet velocity of a few thousand km s^{-1} can easily provide the observed momentum, and we can safely use the approximation: $\Pi_j \approx A_j V_j^2 \rho_{th}(1 - ff_{rj})$. We regard this constraint on the jet's momentum as powerful evidence for the presence of significant thermal material in Seyfert jets, at least on the kpc scale. To estimate the properties of this thermal material we need additional constraints, provided by the jet's energy flux.

6.2. Jet Energy Flux

When estimating the jet luminosity we assume that there are two main repositories for jet energy: the kinetic energy of the ionized line emitting gas, $E_{ke} = E_{ke,t} + E_{ke,i}$, and the internal energy of the region where the jet deposits most of its energy, E_{lobe} . This region, we assume, contains a mix of relativistic and non-relativistic components in rough pressure balance, giving $E_{lobe} = E_{rel} + E_{nrel}$. Since we need these energies to act as bolometers for the jet, are there any significant energy losses? With the exception of some simple correction factors (see below) we assume not. The largest and most obvious would be radiative losses, from either the NLR clouds or from the

jet itself. However, we showed in Paper II that the line emission is powered not by the jet but by the central UV source, and although a small fraction of emission might arise in post shock cooling, at this stage we choose to exclude L_{em} entirely from the jet’s energy analysis. Since this is a major difference from previous studies, we discuss its implications further in §7. The jet itself, of course, is unlikely to radiate significantly simply because of its low density. What about the energy which must be dissipated when a light jet hits and accelerates a denser medium? We assume that this energy ultimately contributes to the expanding lobe, and is therefore included in E_{lobe} . Finally, for the regions to act as efficient bolometers, the jet must terminate and dump all its energy within them. While this is probably true for W-lobe and W-knot, it is probably *not* true for E-fan, since the radio source appears deflected rather than stopped by that region. The weakness of the deflected emission gives us hope that the error introduced might be a factor ~ 2 , and we proceed with this potential uncertainty in mind.

Consider now the jet energy required to yield E_{ke} and E_{lobe} . For E_{ke} there are essentially no correction factors since any jet energy dissipated while accelerating the clouds shows up in the internal energy of the lobe. The jet energy used to generate E_{lobe} we derive from E_{rel} using Equations A22 and A26, with correction terms for synchrotron and adiabatic losses. Synchrotron losses are $\sim 20\%–50\%$ (estimated from $(L_{rad} \times t_{age})/E_{rel}$ for each region), giving correction factors $\alpha_{syn} \simeq 1.0–1.5$. The adiabatic correction is typically $\alpha_{ad} \sim 2$ and represents the energy needed to create the radio source cavity within the surrounding ISM. A potential uncertainty relates to the unknown relativistic filling factor, ff_{rl} . In the standard analysis, $E_{rel} \propto ff_{rl}^{3/7}$, from the combined dependence of $P_{rel} \propto ff_{rl}^{-4/7}$ (Equation A21) and the linear dependence of E_{rel} on source volume (Equation A22). However, by including a non-relativistic component (for which $E = \frac{3}{2}PV$) with the relativistic component (for which $E = 3PV$) we mute the dependence of E_{lobe} on ff_{rl} , such that (Equation A26): $E_{lobe} = \alpha_{ff} E_{rel,ff=1}$ where $E_{rel,ff=1}$ is the usual value of E_{rel} evaluated with $ff_{rl} = 1$, and $\alpha_{ff} = ff_{rl}^{-4/7}(1 + ff_{rl})/2$ which is $1/2/7$ for $ff_{rl} = 1.0/0.1/0.01$. Thus, as long as the filling factor for relativistic particles isn’t too small, this multiplicative factor is $\alpha_{ff} \sim 1$ –few. The total energy required to generate the lobe is therefore $\sim \alpha_{syn}\alpha_{ad}\alpha_{ff} \times E_{rel,ff=1}$, where $\alpha_{syn}\alpha_{ad}\alpha_{ff} \sim 2–10$.

Combining these two energy estimates we have for the jet luminosity, L_j :

$$L_j t_{age} \approx E_{ke} + \alpha_{syn}\alpha_{ad}\alpha_{ff} E_{rel,ff=1} \quad (3)$$

From Table 2 we have for the three regions $\log E_{ke}/t_{age} \simeq 40.0/40.1/39.7 \text{ erg s}^{-1}$ and $\log E_{rel}/t_{age} \simeq 40.1/39.7/40.0 \text{ erg s}^{-1}$, giving a rough estimate for the jet luminosity of $\sim 2–10 \times 10^{40} \text{ erg s}^{-1}$. Note that for Mkn 78, although E_{ke} and E_{rel} are similar, it is E_{rel} which contributes most to our estimate of the jet energy because of the correction factors. In this and possibly other cases, the radio source may therefore act as a bolometer for the jet. Indeed, this is an assumption in the estimate of jet synchrotron efficiency, $R_{syn} = L_{rad}/L_j \approx (\kappa_\nu$ in Bicknell’s 1994 treatment), given by Equations A27 and A28 (see

§6.9).

We note that at $\sim 10^{40.5} \text{ erg s}^{-1}$, the jet luminosity is $\lesssim 1\%$ of the photon luminosity entering the regions. This is consistent with our simpler result from §5.3 based on measured energies, but is astrophysically more important since it addresses the energies entering, not merely evident in, the regions. Furthermore, after correcting for geometry (*two* jets; regions subtending $\sim 5–10\%$ of 4π) we note that the AGN itself has jet luminosity $\lesssim 0.1\%$ of its photon luminosity. This ratio, of course, is likely to lie at the heart of the distinction between radio quiet and radio loud AGN. With typical radio powers $\sim 10^3–10^4$ times greater (and similar synchrotron efficiencies, see §6.9), this confirms the possibility that radio loud AGN have roughly equal luminosities in jets and photons — a scenario favoured in several theoretical models (e.g. Falke & Biermann 1995).

While the jets in radio loud AGN may well be dominated by relativistic material, our baseline assumption for the jet in Mkn 78 is that it contains at least some non-relativistic (thermal) material. In this case the energy of the jet resides in two forms (Equation A39): the kinetic energy of the thermal component, and the internal energy of both the thermal and relativistic components. Can we ascertain which is dominant in Mkn 78? Consider the ratio of these two components: $R_{ke} = KE/E_{int}$, as given by Equation A41. The RHS of that Equation has the virtue that it does not rely on our primary unknowns, ρ_{th} or V_j , but on quantities we have some handle on, namely Π_j , A_j , and $P_{rel,ff=1}$. From Table 2 we have for the three regions: $R_{ke} \sim 10/2/1$. Thus, we find that, to first order, the jet luminosity in Mkn 78 is dominated by the kinetic energy of the thermal component. Furthermore, if we trust the reality of the decrease in R_{ke} for the three regions, it suggests the jet flow converts kinetic energy to internal energy as it moves out into the NLR — a plausible possibility.

Combining this result with the previous section, we have learned that on scales $\gtrsim 100 \text{ pc}$ the jet in Mkn 78 has a thermal component which dominates both its inertia and its energy — it is primarily a thermal jet in which the relativistic component is simply carried along for the ride. Having established the basic character of the jet, we can now evaluate a number of its other properties.

6.3. Jet Velocity

As usual, the ratio of an energy and a momentum gives a velocity. From Equations A40 and A41 we have:

$$\frac{2L_j}{\Pi_j} = V_j + \frac{5P_{rel}}{\rho_{th}V_j} \frac{(1+0.6ff_{rlj})}{(1-ff_{rlj})} = V_j \left(1 + \frac{1}{R_{ke}} \right) \quad (4)$$

where the second term comes from the fact that the jet has internal as well as kinetic energy, and in its absence we recover the usual relation $2L/\Pi = V$. As mentioned above, jet energy is dominated by its kinetic energy and so to first order we can use the simple relation.

We can now use our earlier estimates for the total jet momentum and energy to estimate its velocity:

$$\begin{aligned} \frac{2L_j}{\Pi_j} &\simeq \frac{1}{\alpha_{drag}\alpha_{cf}} \frac{2E_{ke}}{G_{em}} + \frac{\alpha_{syn}\alpha_{ad}\alpha_{ff}}{\alpha_{drag}\alpha_{cf}} \frac{2E_{rel}}{G_{em}} \\ &\simeq (0.2–0.5) \frac{2E_{ke}}{G_{em}} + (1–6) \frac{2E_{rel}}{G_{em}} \end{aligned} \quad (5)$$

For the three regions, we have $2E_{ke}/G_{em} \simeq 400 - 630/400/250 \text{ km s}^{-1}$, and $2E_{rel}/G_{em} \simeq 200-800/160/500 \text{ km s}^{-1}$, giving a combined estimate for $2L_j/\Pi_j \simeq 300 - 3000 \text{ km s}^{-1}$, and but for the factor $(1 + 1/R_{ke})$ which is of order unity, this is also our estimate of the jet velocity — comparable though probably somewhat larger than the ionized gas velocities. Given the uncertainty introduced by the correction factors, we choose not to interpret any differences between the estimated jet velocity within the three regions.

There is an alternative approach to constraining the jet velocity if we assume that the energy dissipated as the jet accelerates the ionized gas provides the internal energy for the radio source expansion. Since faster jets dissipate more energy then the ratio of E_{lobe} to E_{ke} should throw some light on the jet velocity. Consider a jet of average density $\rho_j = \rho_{th}(1 - ff_{rj})$ and velocity V_j impinging on a cloud of diameter d_c , density ρ_c moving at velocity V_c . The acceleration of the cloud and the energy loss from the jet are:

$$\frac{dV_c}{dt} \approx \frac{\rho_j(V_j - V_c)^2 d_c^2}{\rho_c d_c^3} \quad (6)$$

$$\frac{dE_{loss}}{dt} \approx \frac{1}{2} \rho_j (V_j - V_c)^3 d_c^2 \quad (7)$$

giving

$$\frac{dE_{loss}}{dV_c} \approx \frac{1}{2} (V_j - V_c) \rho_c d_c^3. \quad (8)$$

Integrating from $V_c = 0$ to $V_c = V_{em}$ we have

$$\begin{aligned} E_{loss} &\approx \frac{1}{2} \rho_c d_c^3 (V_j V_{em} - \frac{1}{2} V_{em}^2) \\ &\approx E_{ke,c} \left(\frac{V_j}{V_{em}} - \frac{1}{2} \right) \end{aligned} \quad (9)$$

where $E_{ke,c}$ is the final kinetic energy of the accelerated cloud. Associating this energy loss with the internal energy of the lobe, we have $E_{loss} \approx E_{lobe} \approx \alpha_{syn} \alpha_{ad} \alpha_{ff} E_{rel} \approx (2 - 10) E_{rel}$, giving estimates for $V_j \sim V_{em} \times [(2 - 10) E_{rel} / E_{ke} + \frac{1}{2}]$. Since $E_{rel} \approx E_{ke}$ to within factors ~ 2 then $V_j \sim (1 - ff_{ew}) \times V_{em}$. Basically, since the kinetic energy of the ionized gas and the energy dissipated accelerating it are comparable, then the jet velocity must be of order the gas velocity.

Although these estimates of jet velocity remain uncertain to factors of a few, the conclusion that the jet velocity in Mkn 78 is of order the emission line velocity is, we feel, reasonably robust. Perhaps the most conservative statement would be that we can safely rule out a fast jet of 10^4 km s^{-1} or greater.

6.4. Jet Ram Pressure

The dynamical, or ram, pressure exerted by the thermal component of the jet is:

$$\begin{aligned} P_{j,dyn} &= \frac{\Pi_j}{A_j} \simeq \frac{\alpha_{drag} \alpha_{cf} \Pi_{em}}{A_j} \quad (10) \\ &\simeq 100 \times (2-4) \Pi_{em,33} A_{j,4}^{-1} \times 10^{-10} \text{ dyne cm}^{-2} \end{aligned}$$

which can also be expressed in terms of the pressure in the relativistic component:

$$\frac{P_{j,dyn}}{P_{rel}} = \frac{\rho_{th} V_j^2 (1 - ff_{rj})}{P_{rel}} \approx 5 (1 + 0.6 ff_{rj}) R_{ke} \quad (11)$$

and we learn that the dynamical pressure is usually somewhat greater than the internal jet pressure. For our three regions, for example, we have $P_{j,dyn}/P_{rel} \sim 20 - 40/5 - 10/3 - 6$, where the drop with radius is perhaps expected as the regions get wider. These dynamical pressures are not only greater than the internal region pressure, but they are also greater than the radiation pressure. Thus, although in §5.4 we noted the possible importance of radiation pressure, given its similarity to the pressure in the relativistic component, we now see that probably *neither* play the dominant role in accelerating the ionized gas — as suspected all along, it is ram pressure from the thermal material within the jet which dominates the acceleration.

6.5. Shock Speeds

Since jet ram pressure determines shock velocities in emission line clouds (i.e. $\rho_j V_j^2 \approx \rho_{em} V_{sh}^2$), we can derive these shock speeds: $V_{sh} \approx V_{em} (ff_{em} \alpha_{drag} \alpha_{cf})^{1/2} \approx 0.03 - 0.1 V_{em} \approx 10 - 50 \text{ km s}^{-1}$. As discussed further in §7, these are considerably less than previous estimates, which in effect assumed $V_{sh} \approx V_{em}$ to derive much higher jet ram pressures. In our analysis, it becomes clear why little shocked line emission is seen: our jet is too weak to drive sufficiently high shock velocities to generate high luminosity high excitation line emission.

6.6. Jet Mach Number

It is unclear how to treat the sound speed, c_s , of our two-component jet, since relativistic and thermal gases have very different sound speeds: $c_{s,r}^2 \approx c^2/3$ and $c_{s,th}^2 \approx \gamma P/\rho$ ($\gamma = 5/3$ is the adiabatic index of the thermal gas). If the two components are intimately mixed we simply use the reduced average density: $c_s^2 \approx \gamma P/\rho(1 - ff_{rj}) = c_{s,th}^2/(1 - ff_{rj})$. If, however, the two components are poorly mixed (but acoustically coupled), then we use the weighted average sound speed $c_s \approx c_{s,r} c_{s,th} / [c_{s,th} ff_{rj} + c_{s,r} (1 - ff_{rj})] \approx c_{s,th} / (1 - ff_{rj})$. These differ by a factor $(1 - ff_{rj})^{-1/2}$ which is modest unless $ff_{rj} \approx 1$, which is unlikely since the jet is thermally dominated. We therefore adopt the first case, giving the jet's Mach number:

$$\begin{aligned} M^2 &= V_j^2 / c_s^2 \approx \frac{\rho_{th} V_j^2 (1 - ff_{rj})}{\gamma P_{rel}} \\ &\approx \frac{3 P_{j,dyn}}{5 P_{rel}} \approx 3 (1 + 0.6 ff_{rj}) R_{ke} \end{aligned} \quad (12)$$

Taking values for $P_{j,dyn}/P_{rel}$ from the previous sections, we find jet Mach numbers in the three regions of $\sim 5/2.5/2$. We learn that the jet is transonic as it traverses the emission regions. These low Mach numbers are also consistent with the jet's poor collimation and easy disruption, as found for typical FR-I jets which decollimate and start turbulent entrainment when they become transonic (Bicknell 1994).

6.7. Jet Density and Temperature

We can now estimate the density of the thermal component of the jet:

$$\begin{aligned} n_{th} &\simeq \frac{\Pi_j}{A_j V_j^2 m_p (1 - ff_{rj})} \simeq \frac{\alpha_{drag} \alpha_{cf} \Pi_{em}}{A_j V_j^2 m_p (1 - ff_{rj})} \text{ cm}^{-3} \\ &\simeq (1 - 2) \times \Pi_{em,33} A_{j,4}^{-1} V_{j,3}^{-2} (1 - ff_{rj})^{-1} \text{ cm}^{-3} \end{aligned} \quad (13)$$

Allowing for the uncertainty in V_j , a conservative range for the jet density is therefore $0.1 \lesssim n_{th} \lesssim 5 \text{ cm}^{-3}$. It is an important result, therefore, that this density is comparable to the low density, high filling factor phase of the ISM, and its appearance in the jet is consistent with its origin as entrained ISM. Stated slightly differently, the jet density ratio $\eta \sim 1$, is unusually high compared with most extragalactic jets. Clearly, at least on the kpc scales, this Seyfert jet is a heavy one, and future simulations of Seyfert jets should probably concentrate on these high density ratios.

Since one of our assumptions is that the thermal component is in pressure equilibrium with the relativistic component, we can now estimate the temperature of the thermal component: $T_j \sim P/kn_{th} \sim 7.2 \times 10^5 P_{rel,-10} n_{th}^{-1}$ K. Substituting for n_{th} from above, and expressing the jet velocity as an equivalent (thermalized) temperature $T_{Vj} \approx 4.0 \times 10^7 V_{j,3}^2$ K, we find that the ratio of the jet's temperature to what we expect for material thermalized as it is entrained at the jet speed is:

$$T_j/T_{Vj} \sim 0.012 P_{rel,-10} \Pi_{em,33}^{-1} A_{j,4} (1 - ff_{rj}) \quad (14)$$

Taking values from Table 2 we find for the three regions $T_j/T_{Vj} \sim 0.1 - 0.3/0.5/0.7 (1 - ff_{rj})$. Within the considerable uncertainties, we feel these values are basically consistent with the scenario just described: namely, that ISM material has been entrained by the jet and acquires a temperature somewhat below full thermalization at the jet velocity. This is, of course, equivalent to our earlier conclusion that the region's internal pressure was somewhat lower than the jet flow's ram pressure.

6.8. Jet Mass Flux

How much mass is transported by the jet? In terms of our fiducials, we have:

$$\begin{aligned} \dot{M}_j &\simeq \frac{\Pi_j}{V_j} \simeq \frac{\alpha_{drag} \alpha_{cf} \Pi_{em}}{V_j} \\ &\simeq 0.16 \times (2 - 4) \Pi_{em,33} V_{j,3}^{-1} M_\odot \text{ yr}^{-1} \end{aligned} \quad (15)$$

or if we sum over the region lifetime:

$$\begin{aligned} M_{j,tot} &= \dot{M}_j t_{age} \approx \frac{\alpha_{drag} \alpha_{cf} G_{em}}{V_j} \\ &\approx M_{em} \frac{\alpha_{drag} \alpha_{cf}}{\alpha_{syn} \alpha_{ad} \alpha_{ff}} \frac{E_{ke}}{E_{rel}} \end{aligned} \quad (16)$$

where we have used the fact that $G_{em}/V_{em} = M_{em}$ and $V_j/V_{em} \approx \alpha_{syn} \alpha_{ad} \alpha_{ff} E_{rel}/E_{ke} + \frac{1}{2}$ (and we ignore the final $\frac{1}{2}$). Gathering the α factors, and recalling that $E_{rel}/E_{ke} \sim 1$, we find the jet brings into the emission region an amount of mass of order the ionized mass we see

via emission lines. Where does this gas end up? Since $n_{th} \sim 10^{-3} n_{em}$ and $ff_{em} \sim 10^{-2} - 10^{-4}$, then the thermal material brought in by the jet may simply fill the rest of the volume occupied by the emission line region.

6.9. Jet Synchrotron Efficiency

How efficient is the jet at converting energy into relativistic particles and synchrotron emission? The parameter $R_{syn} = L_{rad}/L_{jet}$ characterizes this efficiency. A simple substitution for L_j from S6.2 and L_{rad} from Table 2 gives $R_{syn} \sim 0.03 - 0.1$. It is instructive, however, to look at the explicit expression for R_{syn} given by Equation A27, which uses E_{lobe} as a lifetime bolometer for the jet. Although this ignores that part of L_j which ends up in the kinetic energy of the ionized gas, it is nevertheless a good approximation since, as we showed in S6.2 Equation 3, $E_{lobe} \sim \alpha_{syn} \alpha_{ad} \alpha_{ff} E_{rel}$ dominates over E_{ke} by factors of $\sim 2 - 10$. Setting $\alpha_r \sim 0.8$, $f_{ad} \sim 0.5$ and $a = 2$ in Equation A27, we have

$$\begin{aligned} R_{syn} &\approx 0.23 \times F_{ff} B_{-4}^{3/2} t_{age,6} \\ &\approx 0.10 \times F_{ff} P_{-10}^{3/4} t_{age,6}, \end{aligned} \quad (17)$$

where B_{-4} and P_{-10} are evaluated assuming $ff_{rl} = 1$ and the geometrical term $F_{ff} = ff_{rl}^{4/7} / (ff_{rl} + 1) = 0.02 - 0.5$ for $ff_{rl} = 10^{-3} - 1$. For the three regions we find similar values for $R_{syn} \approx 0.21/0.24/0.24 \times F_{ff}$, and assuming a modest relativistic filling factor we recover our basic conclusion that the jet converts a few percent of its energy into synchrotron emission.

This value is, in fact, similar to estimates for other classes of jet. Estimates of radio source age and magnetic field strength for compact (CSS and GPS) radio galaxies (e.g. O'Dea 1998), Seyferts (Wilson ref-please), and extended (FRI, FRII) radio galaxies (e.g. Laing et al. 1999) suggest increasing ages ($\log t_{age} \sim 4 - 6$; $5.5 - 6.5$; $6.5 - 7.5$ yr) and decreasing fields ($-\log B_{min} \sim 3.5 - 4.5$; $4 - 5$; $4.5 - 5.5$ Gauss) respectively. From these we find similar synchrotron efficiencies: $R_{syn} \sim 1$ –few% for the three classes of AGN. While this similarity supports, to some extent, the credibility of our Mkn 78 analysis it does, however, also raise the interesting question of why the synchrotron efficiency of two rather different kinds of jet should be so similar: the thermally dominated jets of Seyferts, and the relativistically dominated jets of radio galaxies. As argued in §9 it may simply require that both jets include a relativistic component and are dynamically confined.

Note that our analysis differs somewhat from that of Bicknell et al. (1998). Because their estimates of L_{jet} are $\sim 10^2 - 10^3$ times higher than ours (see §7 below) their estimates of jet synchrotron efficiency are correspondingly lower: $R_{syn} \sim 10^{-4}$ (or equivalently, $\kappa_{1,4} \approx 10^{-13} - 10^{-15}$, see Equation A28 and their Figure 2). With such low values for R_{syn} , they need to interpret Equation A27 (the radio lobe ‘‘bolometer’’ relation) as implying sub-equipartition fields and/or low relativistic filling factor (ie significant thermal component). In our analysis, the need for a thermal component arises because of the jet's high momentum, while the jet's lower power implies a ‘‘normal’’ synchrotron efficiency and normal equipartition fields.

7. COMPARISON WITH PREVIOUS WORK

Our results for the jet properties in Mkn 78, and by implication other Seyfert jets, are important and need critical assessment. Lets therefore review our assumptions and then compare these with other approaches.

Our primary assumption is that the jet plays a major role accelerating the ionized gas. Momentum considerations then imply the jet must contain at least some thermal (i.e. not relativistic) gas, at least on the scales of the emission regions. Our second assumption is that the jet's energy is lost to the kinetic energy of the ionized gas and the creation of the radio lobe – they can therefore act as a crude bolometer for the jet. Combining these estimates for energy and momentum fluxes we find a modest jet velocity, perhaps a few times that of the emission line velocities. With these basic characteristics, other properties fall into place: the density of the thermal component is similar to that of the ISM; the jet's ram pressure dominates over internal or radiation pressures; the jet transports a modest mass over its lifetime, comparable to the ionized gas; and the jet's synchrotron efficiency is similar to that of other more powerful extragalactic jets. Our third assumption is that the thermal and relativistic phases are in rough pressure balance. This gives us access to the jet's total internal energy; reveals mildly supersonic Mach numbers with jet temperatures somewhat below the thermalization temperature; and confirms that the jet's energy is dominated by the kinetic energy of the thermal component.

It is important to contrast these results with those of Bicknell et al. (1998). Although our approach follows that work, their initial assumption is quite different: that the emission line luminosities and velocities arise directly from clouds shocked by a jet. For Seyferts, high emission line luminosities translate directly into high jet powers: $L_j \sim 100L_{[\text{OIII}]}$, where the factor is derived from detailed shock models. Since, for typical Seyferts, $L_{em} \sim 10L_{[\text{OIII}]} \sim 10^3L_{ke} \sim 10^3L_{rel}$ then jet powers estimated from emission lines are $\sim 10^3 - 10^4$ times higher than those estimated from L_{ke} or L_{rel} . Jet momenta derived from emission lines are also higher, but not by as large a factor: jet ram pressure is assumed to balance post shock pressures in emission line clouds, $\rho_j V_j^2 \approx \rho_{cl} V_{sh}^2$. Jet momenta Π_j can then be derived either straightforwardly assuming $V_{sh} \approx V_{em}$, $n_{cl} \approx n_{em}$, and $A_{sh} \approx A_{em}$; or using shock models to calibrate shock luminosities, allowing $L_{H\alpha}$ to be used to estimate post shock pressures and hence jet momenta (sometimes additional geometrical factors are required if a jet is deflected rather than fully blocked, as with Bicknell et al's analysis of cloud C in NGC 1068). Ultimately, their method gives higher values of Π_j by factors $\sim cf/(\alpha_{drag}\alpha_{cf}ff_{em}) \sim 10^2$, and consequently their derived jet velocities, $V_j \sim 2L_j/\Pi_j$, are $\sim 10 - 100$ times larger than ours, more like $0.05c - 0.3c$. Compared to our jets, these faster jets also have significantly lower densities, higher ram pressures, higher temperatures ($\sim 10^9\text{K}$), lower synchrotron efficiencies, but similar mass transport rates. Of course, as in our analysis, the relatively high inferred jet momenta also demand the presence of a thermal component.

The essential difference between the two approaches is in the relative importance assigned to radiative shocks. This issue has two distinct contexts. The most impor-

tant concerns the energy budget of the jet. As argued in detail in Paper II, for Mkn 78 (perhaps the archetypal jet-influenced Seyfert) the emission lines do NOT seem to originate from radiative shocks, but instead from gas which is photoionized by UV radiation from the nuclear source. Unfortunately, although the line emission may not be dominated by radiative shocks, some jet energy may still emerge as line cooling, and our estimates of jet energy are strictly lower limits. Since the line emission dominates other energy fluxes by a factor $\sim 10^3$ then even if only a few percent resulted from jet induced cooling this could still dominate the jet energy budget and increase our estimates of L_j by factors of a few (cf. Equation 3: $L_{jet} \approx \alpha_{syn}\alpha_{ad}\alpha_{ff}L_{rel} \approx 2 - 10L_{rel}$). In future it will be important to place strict limits on the contribution of radiative shocks to NLR emission in AGN with jets.

The second context is the way in which ionized gas is accelerated. In almost all earlier studies, emission line velocities are treated as if they arise impulsively by momentum driven shocks, allowing one to invoke the condition: $\rho_j V_j^2 \approx \rho_{em} V_{em}^2$. This kind of impulsive acceleration is analogous to that experienced by a golf ball being struck by a golf club. Not surprisingly one derives a high jet velocity and very high jet ram pressure: $P_{ram,-10} \approx 1700 n_{em,3} V_{em,2}^2$. Instead, we frame momentum conservation globally rather than locally, by equating the total jet momentum flux with the total ionized gas momentum flux. The drawback of this approach, perhaps, is that we introduce uncertainties in the region lifetime and its global structure. The benefit, however, is that we do not need to specify the acceleration mechanism — we are no longer committed to impulsive shock acceleration as the origin of NLR jet related velocities. The equivalent momentum balance condition is:

$$\Pi_j \approx \rho_{th}(1 - ff_{rj})A_j V_j^2 \approx \alpha_{drag}\alpha_{cf}\Pi_{em} \quad (18)$$

$$\Pi_{em} \approx \frac{G_{em}}{t_{age}} \approx \frac{M_{em}V_{em}^2}{D_{em}} \approx \rho_{em}ff_{em}V_{em}^2 A_{em} \quad (19)$$

which, on setting $A_j \approx A_{em}$, gives:

$$\rho_{th}(1 - ff_{rj})V_j^2 \approx \rho_{em}ff_{em}V_{em}^2 \times \alpha_{drag}\alpha_{cf} \quad (20)$$

which closely matches the shock condition but replaces the undiluted jet and emission cloud densities with their global (filling factor) averages. Because the cloud filling factors are small, $ff_{em} \sim 10^{-3}$, we immediately see that our approach to momentum balance gives jet velocities and ram pressures that are significantly lower than those of Bicknell et al's analysis. Returning to the golf analogy, the golf ball gradually achieves its final velocity after a sustained wind blows it off the tee and across the (frictionless) fairway. Using canonical parameter values to illustrate (e.g. $n_{em} \sim 10^3$, $n_j \sim 1$, $ff_{em} \sim 10^{-3}$), our condition gives $V_j \approx 1.7V_{em}$ while the shock condition gives $V_j \approx 30V_{em}$. Similarly, our condition gives jet ram pressures which are lower by a factor $ff_{em}\alpha_{drag}\alpha_{cf} \sim 0.01 - 0.001$. Indeed, since the jet ram pressure determines the shock velocity in emission line clouds, i.e. $\rho_j V_j^2 \approx \rho_{em} V_{sh}^2$ we find much weaker shocks (see also §6.5): $V_{sh} \approx V_{em}(ff_{em}\alpha_{drag}\alpha_{cf})^{1/2} \approx 0.03 - 0.1V_{em} \approx 10 - 50 \text{ km s}^{-1}$. Of course, as discussed

in §5.5, these lower ram pressures can nevertheless generate velocities $\sim V_{em}$, but more gradually over the region lifetime.

Although we feel there is good evidence against invoking radiative shocks to estimate jet energy flux (see above and Paper II), it is less clear whether to prefer local (shock), or global, momentum balance conditions to estimate jet momentum flux. Overall, however, we feel a case can be made to prefer the global condition. The argument rests on the fact that we observe coherent trends in velocity across the emission regions. Since much emission evidently arises independently of shocks (e.g. outside the flow regions or in objects with no prominent radio source), then any shock accelerated gas at a jet/cloud interface will generate high velocity gas in the vicinity of unaccelerated gas. Hence, if shock acceleration is important we expect to see high and low velocity emission essentially cospatial. In practice, however, we find the emission regions show more or less coherent global patterns in both emission and velocity — knots move with well defined, but different, velocities, while diffuse regions often show velocity gradients. This velocity/structure coherence more closely matches that of gas which is experiencing gradual but systematic acceleration, rather than in situ instant acquisition of high velocity. In these circumstances, one should not use the fast shock boundary condition to estimate the jet ram pressure.

In summary, in trying to pin down the properties of the bipolar flow in Mkn 78, we have avoided both the use of emission line luminosity as tracer of jet luminosity, or the picture in which gas acceleration occurs impulsively via fast shocks. Instead, we use the energy stored in the radio source and the motion of the ionized gas to infer the jet luminosity, and we assume that the jet shares its momentum with the ionized gas over the region lifetime. In empirical terms, we take seriously the results which suggest that jet interactions do not power the emission lines, and we feel the overall distributions of velocity and line emission favour a more global, rather than local, acceleration process. The new estimates of jet energy and momentum show it to be much less powerful, with a velocity up to a few times the emission line velocities, and with internal density similar to that of the low density ISM phase. Stated more emotively, and memorably, compared to the jets of Bicknell et al, ours is a kinder gentler jet.

8. THE NUCLEAR JET

When discussing the jet flow in Mkn 78 it is important to distinguish between at least four lengthscales: the jet base within a few $\times 10^3$ Schwarzschild radii where, presumably, the jet is created and accelerated; the parsec scale components which probably contribute to the unresolved radio core; the ~ 100 pc scale jet visible behind the dust lane; and the kpc scale flows associated with the outer emission regions. Our analysis to this point has focussed mainly on the kpc-scale flow, which we find to be dominated by thermal gas moving at speeds $1\text{--}few \times V_{em}$.

An important question is whether the innermost jet, either the jet base or pc-scale jet, could be dominated by purely relativistic gas, as is thought to be the case in radio galaxies. In this scenario, the thermal material must be entrained before the jet emerges into kpc scales. Al-

ternatively, could jets in radio quiet objects be thermally dominated from the outset? Our data shed some light on this issue, and suggest that Seyferts jets are indeed created as thermally dominated flows.

8.1. A Purely Relativistic Nuclear Jet ?

Can a nuclear jet containing *only* relativistic material yield the observed kpc-scale flow properties while also conforming to the observed core properties? Consider first the unresolved steep spectrum radio core: it has a 3.6 cm flux of 3.8 mJy and a size $< 0''.1$. Assuming this core emission arises from a small jet of length D_{cj} pc and crosssection A_{cj} pc² (“cj” = core-jet), then using $\alpha_r = 0.88$, Equations A19–A21 give a pressure $P_{cj} \approx 4.5 \times 10^{-6} (a/ff_{rl})^{4/7} (A_{cj} D_{cj})^{-4/7}$ dyne cm⁻². Setting $ff_{rl} = 1.0$ (pure relativistic gas) and $a = 2$ (equal energy in ions and electrons), we find from Equations A38 and A39:

$$\Pi_{cj} \approx 1.9 \times 10^{32} \frac{A_{cj}^{3/7} \beta_{cj}^2}{D_{cj}^{4/7}} \left[\frac{4}{3} + \frac{18}{(A_{cj} D_{cj})^{1/7}} \right] \text{ dyne} \quad (21)$$

$$L_{cj} \approx 2.7 \times 10^{42} \frac{A_{cj}^{3/7} \beta_{cj}^2}{D_{cj}^{4/7}} \left[\frac{2.7}{\beta_{cj}} + \beta_{cj} \right] \text{ erg s}^{-1} \quad (22)$$

where the first term in each bracket comes from the internal energy and the second term from the rest mass. (Note: in §6, where thermal material is present, we can ignore the relativistic restmass, but here we cannot). The jet dimensions are constrained by being unresolved in the natural weight data; being optically thin at 3.6 cm; and having sensible aspect ratio; which together yield $0.01 \text{ pc} < D_{cj} < 30 \text{ pc}$ and $D_{cj}/30 < A_{cj}^{1/2} < D_{cj}/3$. These give geometrical factors in Equation 21 in the range 2 – 15, giving a momentum for the core jet of $\Pi_{cj} \sim (0.4 - 3) \beta_{cj}^2 \times 10^{33}$ dyne. Since the kpc-scale jet flow has $\Pi \approx (2 - 5) \times 10^{33}$ dyne (see §6.1), then momentum conservation demands that a relativistically dominated core jet must also be fast, with $\beta_{cj} \sim 1^6$. With $\beta_{cj} \sim 1$, Equation 22 gives a very high jet luminosity: $L_{cj} \sim (0.1 - 1) \times 10^{43}$ erg s⁻¹. Is such a high luminosity fast jet plausible? Almost certainly not, for several reasons. First, whenever pc-scale proper motions have been measured in Seyferts they are significantly sub-relativistic, with $\beta \lesssim 0.1$ (e.g. Roy et al. 2002). Mkn 78 would therefore need to be an exception if it had a relativistic pc-scale bulk flow. Second, the transition from a fast light core-jet to a slow heavy kpc-scale jet (due to mass loading) necessarily involves energy dissipation. For Mkn 78, a relativistic core-jet with luminosity $\sim 10^{42.5}$ erg s⁻¹ becomes a kpc-scale jet with luminosity $\sim 10^{40.5}$ erg s⁻¹ (see §6.2), and hence the core-jet must dump almost all its energy while it is still in the core. A luminosity of $10^{42.5}$ erg s⁻¹ approaches the combined FIR and emission line luminosities of the entire region and could not easily be hidden. One might argue that core-jet dissipation actually powers the FIR and line emissions, but they are already well explained as arising from reprocessed nuclear UV radiation. A stronger argument against significant jet dissipation in the core is the absence of associated

⁶ Adopting the fully relativistic form of Equation A34 does not significantly affect this conclusion

radio emission. Quantitatively, it requires $R_{syn} \sim 10^{-3}$, which would be significantly below typical values for both Seyferts and radio galaxies (see §6.9).

Essentially the same arguments apply to the jet-base region $\lesssim 1000R_s$ ($\lesssim 0.01$ pc for $10^8 M_\odot$ black hole), though now we demand a radio flux sufficiently below the pc-scale flux to go unnoticed (say, $\lesssim 1$ mJy). Pushing Equations 21 and 22 into smaller regions once again demands a high luminosity fast jet ($\beta \sim 1$). Loading and slowing this jet to match the kpc-scale properties would again involve prodigious energy dissipation with obvious observational consequences, especially in the radio.

In summary, the fact that we observe a thermally dominated high momentum but low luminosity kpc-scale jet effectively rules out a relativistically dominated jet base. Relativistic plasma has such low inertia that only very fast luminous jets carry significant momentum. In this case, the transition to a slow moving thermally dominated flow following mass entrainment results in almost complete loss of jet energy. This energy dissipation would be noticed, especially in the radio which is, of course, notably weak in radio quiet objects such as Seyfert galaxies.

8.2. A Thermally Dominated Nuclear Jet ?

The difficulty of finding a plausible relativistic nuclear jet contrasts with the ease of finding a thermally dominated nuclear jet. Setting $ff_{rj} \sim 0$ in Equations A38? and A39, we find $\Pi_{cj} \simeq 1.6 \times 10^{29} A_{cj} V_{cj,3}^2 n_{th}$ dyne, $L_{cj} \simeq 8.0 \times 10^{36} A_{cj} V_{cj,3}^3 n_{th} (1 + 3.1 M^{-2})$ erg s⁻¹ (M is the jet Mach number which enters through the internal energy and substituting $P_{-10} = 100 n_{th} V_3^2 M^{-2}$ for thermal gas of adiabatic index 5/3). Tying this to the kpc-scale jet we have $\Pi_{cj} \sim \Pi_{kpc} \sim (2 - 5) \times 10^{33}$ dyne and $L_{cj} > L_{kpc} \sim (2 - 10) \times 10^{40}$ erg s⁻¹, which together give $A_{cj} V_{cj,3}^2 n_{th} \sim (1 - 3) \times 10^4$ and $A_{cj} V_{cj,3}^3 n_{th} > (0.25 - 1.2) \times 10^4$ (here we assume $M \geq 1$, ie the jet's luminosity is principally kinetic). Of the three parameters A, V, n , we have additional constraints: $V_{cj,3} \gtrsim 0.3$ (directly from the previous relations); $V_{cj} > V_{kpc}$ (from mass flux $\dot{M}_{cj} = \Pi_{cj}/V_{cj} < \dot{M}_{kpc} = \Pi_{kpc}/V_{kpc}$); and $A \sim 100$ pc² in the core and $\sim 10^{-4}$ pc² at the jet base. These constraints allow quite reasonable parameters for A, V , and n . For example, a modest jet speed of $V_{cj,3} \sim 5$ gives $n_{th} \sim 10$ cm⁻³ on pc scales, and $\sim 10^7$ cm⁻³ at the jet base. Such a jet has $\dot{M} \sim 0.1 M_\odot$ yr⁻¹, momentum $\sim 10^{33.5}$ dyne, and luminosity $\sim 10^{41.5}$ erg s⁻¹, entirely consistent with modest entrainment and energy dumping as the nuclear jet matures into the somewhat slower and lower luminosity jet that we find on kpc scales.

Could the nuclear jet be *purely* thermal, with little or no relativistic component? Probably not. As shown in §6.9 Seyfert jet synchrotron efficiencies are comparable to those of both extended and compact radio galaxies, whose jets are thought to be dominated by relativistic material. Contrast this with the thermally dominated flows in starburst driven superwinds which have, relative to their mechanical luminosity, much weaker radio emission, with synchrotron efficiencies $R_{syn} \sim 10^{-4}$. Despite having similar slow, heavy, thermally dominated flows, it would seem that Seyferts and starbursts are fundamentally different in their radio production efficiency. Why might this be? Since efficient particle reacceleration requires a pre-existing popula-

tion of relativistic particles, a plausible explanation is that the Seyfert flows simply have more relativistic material at the outset.

Having established that both thermal and relativistic material are likely to be present in the nuclear jet, can we further constrain their relative amounts, i.e. if ff_{rl} is neither 1 or 0, what is it? Given the various uncertainties a detailed analysis at this stage isn't warranted. We can, however, give some illustrative values based on the example given above. Choosing Mach numbers of 10 at the jet base and 5 on the pc scale, the jet has a thermal pressure of $P_{-10} \sim 2.5 \times 10^8$ and 10^3 in the two regions. Adopting a jet aspect ratio of 5:1 and equating the relativistic and thermal pressures, we find (Equations A20, A21) radio luminosities for the two regions of: $L_{rad} \approx 6.4 \times 10^{31} (ff_{rl}/a) V_{pc^3} P_{-10}^{7/4} = 1.6 \times 10^{41} (ff_{rl}/a)$ and $5.7 \times 10^{40} (ff_{rl}/a)$ erg s⁻¹. Taking $a = 2$ and demanding 3.6 cm fluxes < 1 mJy (jet base) and ~ 3.8 mJy (pc-scale jet), we find $ff_{rl} < 0.02$ and 0.2 for the two regions. While we do not consider this to be a derivation of ff_{rl} , nevertheless we have shown that all observations can be understood by invoking a thermally dominated jet with modest relativistic filling factor. Future theoretical studies of jet production in AGN should consider this kind of thermally dominated jet, in addition to jets dominated by a relativistic phase moving with relativistic bulk velocities.

8.3. The Smallest Resolved Scales

Moving out to consider RW-ijet, the innermost resolved jet, lets briefly consider its asymmetry. Notice that the brighter, western, side corresponds to the side with blueshifted [OIII] emission, at least consistent with the a Doppler origin of the radio asymmetry. If true, this would clearly indicate very high jet speeds on scales $\lesssim 100$ pc. Specifically, for $\beta_j \equiv V_j/c$ moving at angle θ to the line of sight, we have:

$$\frac{I_{west}}{I_{east}} = \left(\frac{1 + \beta_j \cos \theta}{1 - \beta_j \cos \theta} \right)^{2+\alpha_r} \quad (23)$$

which, for our measured flux ratio $I(\text{RW-ijet})/I(\text{RE-ijet}) \sim 4.7$ (Paper I Table 4), gives $\beta_j = 0.15 - 0.25$ for $\theta = 30^\circ - 60^\circ$. There are three reasons to doubt the applicability of this analysis for Mkn 78. First, of the four other Seyferts with reasonably well defined jets (Mkn 3, Mkn 6, NGC 1068, NGC 4151) none have similar asymmetries, suggesting the asymmetry in Mkn 78 is just a coincidence. Second, in the few cases with VLBI measured proper motions, the inferred speeds are *not* relativistic, but more like $\sim 0.1c$ (?). Third, a jet with $\beta_j \sim 0.2$ and momentum flux $\sim 10^{33}$ dyne has unrealistic properties: if purely thermal it has exceedingly low density $n_{cr} \sim 10^{-6}$ cm⁻³, while if purely relativistic, it has exceedingly high luminosity $L_j \sim 10^{44}$ erg s⁻¹, neither of which are credible.

9. OVERALL FRAMEWORK

Our analysis of the jet and region properties does not make any detailed assumptions about the nature of the jet-gas interaction itself. Rather, we have used simple conservation laws to infer jet properties from region properties. In this section we adopt a more global perspective and try to identify the dominant physical processes that might be

occurring, subject to our findings for the flow properties. Many of these processes have, of course, been discussed elsewhere and we draw on much of this prior work.

[TBD]

10. SUMMARY AND CONCLUSIONS

The overall aim of this project is to understand the interaction between the various gaseous components in a subclass of radio quiet AGN: Seyferts with prominent bipolar, radio-emitting, jet flows. Here we focus on a single object, Mkn 78, chosen because the jet-ISM interaction is both clear and strong and hence, we hope, our findings will generalize to other radio quiet AGN. We have used detailed maps of radio emission, line emission, and velocity field to ascertain the distribution of energy and momentum throughout the region, and this in turn allows us to infer the properties of the jet. We now itemize our conclusions, grouping them by overall theme (including, briefly, results from Papers I and II).

10.1. Overview

1: Our new STIS spectra confirm the basic dynamical scenario presented in Paper I: a bipolar radio-emitting jet flow interacts with line-emitting gas, accelerating and dispersing it.

2: A detailed study of the emission line ratios (Paper II) rules out the importance of shock related ionization, and supports the importance of nuclear UV photoionization.

3: Careful comparison with model calculations suggests that the line emitting gas contains a range of optical depths, including both optically thick and optically thin gas.

4: When measurable, all emission line profiles at a given location are quite similar. This not only strengthens the case against the importance of shock ionization, but also requires the velocity fields of the optically thin and thick components to be similar.

10.2. Region Properties

The entire emission region can be usefully divided into three regions (see Figure 1): (a) “W-knot” is a compact high surface brightness region cospatial with the luminous compact inner radio jet, exhibiting modest velocities; (b) “E-fan” is a more extended, structured, fan-like region located where the radio jet is deflected, and shows significant line-splitting; (c) “W-lobe” is a yet more extended multi-component region cospatial with an extended complex radio lobe, and shows a disordered high amplitude velocity field.

5: The properties of these three regions is consistent with an increase in the duration of jet interaction: recent (W-knot); intermediate (E-fan); old (W-lobe). Qualitatively, the sequence shows systematic increases in: nuclear distance; physical extent; physical structure; velocity amplitude; and velocity structure. Quantitatively, estimates of crossing times support this age increase: $\sim 0.4/4.0/8.2$ Myr for W-knot/E-fan/W-lobe, respectively.

6: Standard analysis shows the regions each contain $\sim 10^6 M_\odot$ of ionized gas with low filling factor but high ($\sim 50\%$) local covering factor.

7: We verify that the (minimum) pressures derived for the radio components not only match those expected for the host galaxy ISM, but also match the pressures derived for the line-emitting components, including their $\sim r^{-1}$ radial dependence. These pressures can also drive the lobe through the ISM at velocities similar to the local [OIII] velocities.

8: For each region, we find the energies of the various components fall into two groups: the intercepted nuclear UV and total line emission completely dominate (by $\times 1000$) over all other energies: the kinetic energy of the ionized gas ($\times 1$); the energy stored in the relativistic component ($\times 1$); the energy associated with lobe expansion ($\times 1$); and the energy radiated by synchrotron ($\times 0.3$). This is entirely consistent with our finding in Paper II that emission lines are powered by nuclear UV radiation, and not by shocks. It also suggests that the relativistic component is involved in accelerating the line-emitting gas.

9: The high momentum of the ionized gas ($\sim 10^{48.5}$ dyne-s) places important constraints on possible acceleration mechanisms. For example, estimates of radiation pressure and/or the internal lobe pressure suggest they are too weak by factors $\sim \times 3$. Add to this the fact that these cannot easily cause both radial and lateral motion, and we infer that these forces probably *don't* dominate the acceleration of the ionized gas.

10.3. kpc-Scale Jet Properties

Although the jet flow itself is not easily observed, we can use the region properties discussed above to infer the properties of the jet. To do this, we make three important assumptions: (a) the jet’s momentum (integrated over the region lifetime) can be derived from the momentum of the ionized gas; (b) the jet’s luminosity (integrated over the region lifetime) can be estimated from the kinetic energy of the ionized gas and the energy stored in the radio lobe; (c) the jet contains both relativistic and thermal material in approximate pressure balance. Armed with these estimates for the jet’s luminosity and momentum flux, and its pressure from radio observations, we can derive most of its properties, at least on kpc scales, to ~ 0.5 dex uncertainty:

10: The jet’s luminosity and momentum flux are $\sim 10^{40.5}$ erg s $^{-1}$ and $\sim 10^{33.5}$ dyne. Both these are dominated by the thermal component of the jet, not its relativistic component. Compared to most radio loud AGN, this is a *weak* jet.

11: The ratio of these gives a jet velocity $\sim 300 - 3000$ km s $^{-1}$, or ~ 1 –few times the emission line velocity. Compared to radio loud AGN, this is a *slow* jet.

12: The velocity and force of the jet yield its density: $\sim 0.1 - 5$ cm $^{-3}$, comparable to the hot high filling factor phase of the ISM, suggesting a jet/ISM density ratio $\eta \sim 1$. Compared to radio loud AGN, this is a *dense* jet.

13: We find the jet’s dynamical (ram) pressure to be significantly higher than its internal (static) pressure, by factors $\sim 30/7/4$ for the three regions. This confirms the jet’s ability to accelerate the ionized gas much more effectively than either static or radiation pressure.

14: Despite these relatively high ram pressures, the impact of the jet on line-emitting gas (of density $\sim 10^2 - 10^3 \text{ cm}^{-3}$) generates only slow shocks, $\sim 10 - 50 \text{ km s}^{-1}$. This is, of course, consistent with our failure in Paper II to find emission-line signatures of fast shocks.

15: The jet is transonic, with Mach numbers $\sim 5/2.5/2$ in the three regions. This is consistent with the overall FR-I morphology and efficient mass entrainment. Equivalently, the jet's thermal component has temperature $\sim 10^{5.5} - 10^{6.5} \text{ K}$, somewhat below a fully thermalized flow.

16: Integrated over the region lifetimes, we find the jet brings about $10^6 M_\odot$ of thermal gas into each region. It is possible that this material provides the regions' low density thermal phase within which the ionized and relativistic components reside.

17: Despite the jet in Mkn 78 being so different from the jets in radio loud AGN, it nevertheless has similar synchrotron efficiency: $R_{syn} \equiv L_j/L_{rad} \approx 1\text{--}few\%$. It is presently unclear why this should be.

10.4. Downplaying the Role of Shocks

Our analysis follows closely the one laid out by Bicknell et al. (1998), but with one crucial difference: having failed to identify shock signatures in Paper II, we choose *not* to use shocks to constrain the jet's properties. In contrast, Bicknell et al. employ shock constraints in two important ways: they derive the jet's luminosity assuming the emission lines are powered by radiative jet driven shocks; and they derive the jet's momentum assuming the emission line velocities are generated impulsively behind these same shock fronts. These two different input assumptions lead to radically different inferred jet properties:

18: Compared to our approach, employing shock constraints yields jet luminosities greater by $\sim \times 10^3$, jet momenta greater by $\sim \times 10^2$, and jet velocities greater by $\sim \times 10$. These jets also have much higher ram pressures and temperatures, and much lower densities and synchrotron efficiencies. Stated simply, our jets are much

weaker, slower, and denser than the jets of Bicknell et al.

19: While we feel our jet has inherently more plausible properties, there is another reason to favour it: across the regions the velocity field appears to vary fairly smoothly. While we assume (statistically) gradual acceleration, Bicknell et al's analysis requires impulsive acceleration yielding high (post-shock) and low (pre-shock) velocities at all locations.

10.5. The Nuclear Jet

Finally, it is possible to place constraints on the jet flow at significantly smaller radii, before it enters the emission-line region. We simply demand that the jet emerges with similar momentum to the kpc-scale jet, at least as much luminosity, and its radio emission must be consistent with the unresolved (weak) synchrotron core.

20: With these assumptions, it seems the nuclear jet cannot comprise purely relativistic material, principally because to provide adequate momentum it would have excessively high luminosity. The nuclear jet must therefore emerge carrying at least some thermal material. While we are unable to estimate the relative amounts of thermal and relativistic material, it seems both must be present.

We have greatly benefitted from conversations with Geoff Bicknell, as well as Robert Liang, Alan Bridle, Craig Sarazin, Roger Chevalier, Joss Bland-Hawthorn, and Gerald Cecil. MW and DJR thank IUCAA, Pune; MSSSO, Canberra; the Astronomy Department, UNSW, Sydney, and the Astronomy Department, Oxford, for hospitality while some of this work was completed. Support for proposal numbers GO5417, GO7404 and GO8459 was provided by NASA through a grant from the Space Telescope Science Institute, which is operated by the Association of Universities for Research in Astronomy, Incorporated, under NASA contract NAS5-26555.

APPENDIX

ESTIMATING REGION PROPERTIES

Here we gather simple parameterized relations used in §5 and §6 to estimate basic physical properties of the various components in the regions. Fiducial values are chosen to be representative of Seyferts in general and Mkn 78 in particular. Symbol definitions are given at the end. In general, a numerical subscript refers to the \log_{10} of the fiducial value, for example $M_{em,6}$ has units of $10^6 M_\odot$.

Emission Line Component

Consider an emission region of size $\theta_{ex} \times \theta_{ey}$ arcsec ($\theta_{ey} < \theta_{ex}$) located Δ_e arcsec (D_e cm) from the nucleus, containing ionized gas of density $n_{em} \text{ cm}^{-3}$ with typical column density $N_{em} \text{ cm}^{-2}$. The total ionized gas mass, filling and local covering factors are:

$$M_{em} \approx \frac{L_{H\beta} m_p}{h\nu_{H\beta} n_{em} \alpha_{H\beta}} \approx 8.0 \times 10^{14} (cz/H_o)^2 F_{H\beta} n_{em,3}^{-1} M_\odot \quad (\text{A1})$$

$$ff_{em} \approx \frac{\text{Vol}(\text{gas})}{\text{Vol}(\text{region})} \approx 5.6(2.9?) \times 10^{11} (cz/H_o)^{-1} F_{H\beta} n_{em,3}^{-2} \theta_{ex}^{-1} \theta_{ey}^{-2} \quad (\text{A2})$$

$$cf_{em} \approx \frac{\text{Area}(\text{gas})}{\text{Area}(\text{region})} \approx ff_{em} \times \frac{D_{region}}{D_{cloud}} \approx 8.4 \times 10^{12} F_{H\beta} n_{em,3}^{-1} \theta_{ey}^{-2} N_{em,21}^{-1} \quad (\text{A3})$$

where the local covering factor refers to the fraction of region area covered by gas (equal to the global covering factor if the region completely surrounds the nucleus; here we take θ_y and D_{region} as the angular and physical scales perpendicular to the direction of the nucleus, and D_{cloud} is a typical cloud diameter).

If the line emitting gas moves radially outwards at an angle ϕ to the plane of the sky, with [OIII] profile central velocity and FWHM V_{em} and W_{em} km s⁻¹, then the total momentum, translational, internal, and thermal energies of the gas are:

$$G_{em} \approx M_{em} V_{em} \text{cosec } \phi \approx 2.0 \times 10^{46} M_{em,6} V_{em,2} \text{cosec } \phi \text{ gm cm s}^{-1} \quad (\text{A4})$$

$$E_{ke,t} \approx \frac{1}{2} M_{em} V_{em}^2 \text{cosec}^2 \phi \approx 1.0 \times 10^{53} M_{em,6} V_{em,2}^2 \text{cosec}^2 \phi \text{ erg} \quad (\text{A5})$$

$$E_{ke,i} \approx \frac{1}{2} M_{em} (W_{em}/2.36)^2 \approx 1.8 \times 10^{52} M_{em,6} W_{em,2}^2 \text{ erg} \quad (\text{A6})$$

$$E_{th} \approx 3/2 N k T \approx 4.1 \times 10^{51} M_{em,6} T_{em,4} \text{ erg} \quad (\text{A7})$$

Turning to radiation and ionization properties, we can estimate the photon energy output from the nucleus using the reprocessed FIR flux (e.g. S_{60} , S_{100} Jy IRAS fluxes). Assuming this originates as a power law ($L_\nu \propto \nu^{-\alpha_o}$, $\alpha_o > 1.0$) which is fully absorbed between ϵ_{low} ($\equiv \lambda_{low}$) and high energy, we have relations for the FIR and UV (ionizing) luminosity, the ionizing photon number rate, the ionization parameter, the ionized (Stromgren) column density, and the radiation pressure (assuming the full spectral range is absorbed). Furthermore, using emission lines we can estimate the gas pressure and total line cooling (calibrated using CLOUDY)

$$L_{IR} \equiv L_{ph} \approx 1.5 \times 10^{39} (cz/H_o)^2 \times [2.6S_{60} + S_{100}] \approx \left(\frac{912}{\lambda_{low}} \right)^{1-\alpha_o} L_{UV} \text{ erg s}^{-1} \quad (\text{A8})$$

$$Q_{ion} \approx \frac{\alpha_o - 1}{\alpha_o} \frac{L_{UV}}{\epsilon_H} \text{ s}^{-1} \quad (\text{A9})$$

$$U_{em} \approx \frac{Q_{ion}}{4\pi D_e^2 n_{em} c} \approx 8.2 \times 10^{-4} \frac{\alpha_o - 1}{\alpha_o} \left(\frac{\lambda_{low}}{912} \right)^{1-\alpha_o} [2.6S_{60} + S_{100}] \Delta_e^{-2} n_{em,3}^{-1} \quad (\text{A10})$$

$$N_S \approx U_{em} c / \alpha_B \approx 1.3 \times 10^{23} U_{em} \text{ cm}^{-2} \quad (\text{A11})$$

$$P_{rad} \approx \frac{L_{ph}}{4\pi D_e^2 c} \approx 2.1 \times 10^{-11} [2.6S_{60} + S_{100}] \Delta_e^{-2} \text{ dyne cm}^{-2} \quad (\text{A12})$$

$$P_{em} \approx n_{em} k T_{em} \approx 1.4 \times 10^{-9} n_{em,3} T_{em,4} \text{ dyne cm}^{-2} \quad (\text{A13})$$

$$L_{em} \approx 10 \times L_{5007} \approx 1.2 \times 10^{51} (cz/H_o)^2 F_{5007} \text{ erg s}^{-1} \quad (\text{A14})$$

From the [OIII] velocity and region size, we can estimate a crossing time, t_{cross} , which we tentatively associate with the age of the interaction, t_{age} . This age can be used to interconvert energies with luminosities, and momenta with forces (mechanical luminosity and force are given as examples):

$$t_{age} \equiv t_{cross} \approx 47100 (cz/H_o) \theta_{ex} V_{em,2}^{-1} \tan \phi \text{ yr} \quad (\text{A15})$$

$$L_{mec} \approx (E_{ke,t} + E_{ke,i}) / t_{age} \quad (\text{A16})$$

$$\Pi_{em} \approx G_{em} / t_{age} \quad (\text{A17})$$

Finally, if a cloud is accelerated by a pressure P to velocity V_{em} over a time t_{age} , it has column density:

$$N_P \approx \frac{P t_{age}}{m_p V_{em}} \approx 1.9 \times 10^{20} P_{-10} t_{age,6} V_{em,2}^{-1} \text{ cm}^{-2} \quad (\text{A18})$$

where P_{-10} and $t_{age,6}$ have units of 10^{-10} dyne cm⁻² ($\log P/k = 5.9$ K cm⁻³) and 10^6 yr respectively.

Relativistic Component

Radio sources gives us access to a relativistic component. A source flux of S_ν Jy at wavelength λ cm with power law form $S_\nu \propto \nu^{-\alpha_r}$ has a total radio luminosity:

$$L_{rad} \approx \int_{\nu_1}^{\nu_2} L_\nu d\nu \approx 1.2 \times 10^{36} S_\nu (1+z)^{3+\alpha_r} (cz/H_o)^2 (30/\lambda)^{\alpha_r} X_1(\alpha_r) \text{ erg s}^{-1} \quad (\text{A19})$$

where the term $(1+z)^{3+\alpha_r}$ is a K correction, and the function $X_q(\alpha) = (\nu_2^{q-\alpha} - \nu_1^{q-\alpha}) / (q-\alpha)$ incorporates the spectrum limits ν_1 and ν_2 GHz (typically 0.01 and 100 respectively). Following Moffet (1975) and Miley (1980) we can derive a number of properties of the radio source. The total energy density includes contributions from relativistic particles and

magnetic fields: $u_{rel} = u_p + u_m$, with $u_p = u_e + u_{ions} = au_e$ where a specifies the contribution of the ions (typically, $a \sim 1 - 100$ with values of 1, 2, or 10 commonly adopted). For a given radio luminosity, u_{rel} has a minimum when $u_m \equiv B_{min}^2/8\pi = (3/4)u_p$, corresponding to approximate equipartition of energy between particles and the field. If we assume the relativistic gas has filling factor ff_{rl} within an ellipsoidal radio source of volume $V \text{ cm}^{-3}$ (angular size $\theta_{rx} \times \theta_{ry}$ arcsec, with depth matching θ_{ry}), we have expressions for the field strength B_{min} , pressure P_{rel} , total lobe energy E_{rel} , radiative loss timescale $t_{1/2}$ for electrons emitting at ν_{GHz} , density of relativistic electrons, n_e , and ratio of rest mass energy to energy in particles and fields (assuming 1 proton per electron):

$$B_{min} \approx 326 \left[\frac{a L_{rad}}{ff_{rl} V} \frac{X_{0.5}(\alpha_r)}{X_1(\alpha_r)} \right]^{2/7} \approx 2.93 \times 10^{-4} \left[\frac{S_\nu}{\theta_{rx} \theta_{ry}} \frac{a(1+z)^{3+\alpha_r} (30/\lambda)^{\alpha_r} X_{0.5}(\alpha_r)}{ff_{rl} \theta_{ry} (cz/H_o)} \right]^{2/7} \text{ Gauss} \quad (\text{A20})$$

$$P_{rel} \approx (1/3) u_{rel} \approx (7/9) (B_{min}^2/8\pi) \approx 0.031 B_{min}^2 \approx 0.031 B_{min,ff=1}^2 ff_{rl}^{-4/7} \text{ dyne cm}^{-2} \quad (\text{A21})$$

$$E_{rel} \approx u_{rel} V ff_{rl} \approx 1.6 \times 10^{56} \theta_{rx} \theta_{ry}^2 ff_{rl}^{3/7} (cz/H_o)^3 B_{min,ff=1}^2 \text{ erg} \quad (\text{A22})$$

$$t_{1/2} \approx 0.68 B_{min}^{-3/2} \nu_{\text{GHz}}^{-1/2} \text{ yr} \quad (\text{A23})$$

$$n_e \approx \frac{4.20 \times 10^3}{a} \frac{X_0(\alpha_r)}{X_{0.5}(\alpha_r)} B_{min}^{5/2} \approx \frac{1.02 \times 10^{-7}}{a} \frac{X_0(\alpha_r)}{X_{0.5}(\alpha_r)} P_{-10}^{5/4} \text{ cm}^{-3} \quad (\text{A24})$$

$$\frac{n_e m_p c^2}{u_{rel}} \approx \frac{68}{a} \frac{X_0(\alpha_r)}{X_{0.5}(\alpha_r)} B_{min}^{1/2} \approx \frac{0.51}{a} \frac{X_0(\alpha_r)}{X_{0.5}(\alpha_r)} P_{-10}^{1/4} \quad (\text{A25})$$

where P_{-10} is P_{rel} in units of $10^{-10} \text{ dyne cm}^{-2}$. Note that B_{min} , P_{rel} , E_{rel} and n_e have relatively modest dependencies on a and ff_{rl} : $a^{2/7} ff_{rl}^{-2/7}$; $a^{4/7} ff_{rl}^{-4/7}$; $a^{4/7} ff_{rl}^{3/7}$; $a^{-2/7} ff_{rl}^{-5/7}$ (for clarity, we sometimes show the filling factor explicitly using subscript $ff = 1$: e.g. $B_{min} \equiv ff_{rl}^{-2/7} B_{min,ff=1}$, or $E_{rel} \equiv ff_{rl}^{-4/7} P_{-10,ff=1}$). Note also that a pure synchrotron emitting plasma has very low inertia, with comparable energy in rest mass and other forms.

We can extend this analysis to consider a radio source in which the remaining volume, $V(1 - ff_{rl})$, contains non-relativistic (thermal) gas in pressure balance with the relativistic component. Since for relativistic gas $u_{rel} = 3P$ and for thermal gas $u_{th} = \frac{3}{2}P$ we have for the total lobe energy:

$$E_{lobe} = u_{rel} V ff_{rl} + u_{th} V (1 - ff_{rl}) \approx E_{rel,ff=1} \times ff_{rl}^{-4/7} (ff_{rl} + 1)/2 \quad (\text{A26})$$

where the multiplicative factor $ff_{rl}^{-4/7} (ff_{rl} + 1)/2$ is relatively insensitive to filling factor, taking values 1/2/7 for $ff_{rl} = 1.0/0.1/0.01$. If E_{lobe} derives from a jet with luminosity L_{jet} entering the lobe for time t_{age} with adiabatic expansion loss factor $f_{ad} \sim 0.5$, we have: $E_{lobe} \approx f_{ad} t_{age} L_{jet}$. This now allows us to estimate the ratio of the radio luminosity to the jet luminosity, $R_{syn} \equiv L_{rad}/L_{jet}$, which is itself closely related to the monochromatic parameter $\kappa_\nu \equiv L_\nu/L_{jet}$ defined in Bicknell et al. (1998), with $\kappa_{1.4}$ referring to the value at 1.4 GHz:

$$R_{syn} \equiv \frac{L_{rad}}{L_{jet}} \approx \frac{f_{ad} t_{age} L_{rad}}{E_{lobe}} \approx 1.1 \times 10^6 \frac{ff_{rl}^{4/7} f_{ad} t_{age,6}}{ff_{rl} + 1} \frac{X_1(\alpha_r)}{a X_{0.5}(\alpha_r)} B_{min,ff=1}^{3/2} \quad (\text{A27})$$

$$\approx 10^9 X_1(\alpha_r) (30/\lambda)^{\alpha_r} \kappa_\nu \approx 1.6 \times 10^{10} \kappa_{1.4} \quad (\text{A28})$$

where $\alpha_r = 0.7$ has been used to evaluate $\kappa_{1.4}$. Note that for spectral indices α_r in the range 0.6 – 0.8, the numerical values for the functions $X_1(\alpha_r)$, $X_{0.5}(\alpha_r)$, and their ratio, span ranges 15 – 9, 9 – 12, and 4.2 – 2.5.

Ambient ISM

A region of area A_{lobe} expanding into the ISM at speed V_{lobe} experiences a ram pressure $P_{ram} \approx \rho_{ism} V_{lobe}^2$ and liberates energy at a rate $L_{exp} \approx \frac{1}{2} \rho_{ism} V_{lobe}^3 A_{lobe}$. If the ram pressure is balanced by the radio source pressure, P_{rel} , we can derive values for the luminosity of the expansion and density of the ISM:

$$L_{exp} \approx P_{rel} V_{lobe} A_{lobe} \approx 2.2 \times 10^{35} P_{rel,-10} V_{lobe,2} \theta_{ry}^2 (cz/H_o)^2 \text{ erg s}^{-1} \quad (\text{A29})$$

$$n_{ism} \approx \frac{P_{rel}}{m_p V_{lobe}^2} \approx 0.60 \times P_{rel,-10} V_{lobe,2}^{-2} \text{ cm}^{-3} \quad (\text{A30})$$

Note that L_{exp} depends only weakly on radio source size: $L_{exp} \propto \theta_{rx}^{-4/7} \theta_{ry}^{6/7} \propto \theta^{2/7}$.

A related approach to constraining the ISM density using a model for the growth of the radio source has been given by Bicknell, Dopita, & O’Dea (1997) who were extending work by Begelman (1996). A jet of luminosity L_j burrows into

an ISM with radial density profile $\rho_{ism} \propto x^{-\delta}$ with value ρ_o (and associated hydrogen density n_o) at fiducial distance x_o . The lobe has average pressure P_l , and its outer edge reaches distance x_e from the nucleus after time t with local overpressure $P_e = \zeta P_l$. Solving for the evolution of the lobe yields expressions for the fiducial ISM density, lobe advance speed, and jet luminosity in terms of the lobe pressure, size and age:

$$n_o \approx P_l \frac{\zeta(5-\delta)^2}{9} (t/x_o)^2 (x_e/x_o)^{\delta-2} \approx 1.4 \times 10^{-3} (5-\delta)^2 P_{-10} t_6^2 x_{o,3}^{-2} (x_e/x_o)^{\delta-2} \text{ cm}^{-3} \quad (\text{A31})$$

$$V_e \approx \frac{3\zeta^{-1/2}}{(5-\delta)} (x_e/x_o)^{(5-\delta)/3} (x_o/t) \approx \frac{2000}{(5-\delta)} (x_e/x_o)^{(5-\delta)/3} (x_{o,3}/t_6) \text{ km s}^{-1} \quad (\text{A32})$$

$$L_j \approx P_l \frac{2\pi(8-\delta)}{\zeta(5-\delta)} t^{-1} x_e^3 \approx 2.9 \times 10^{41} \frac{(8-\delta)}{(5-\delta)} P_{-10} x_{e,3}^3 t_6^{-1} \text{ erg s}^{-1} \quad (\text{A33})$$

where $x_{o,3}$ and $x_{e,3}$ are in units of kpc, and plausible values for $\zeta \sim 2$ and $\delta \sim 1-2$. These relations roughly match those above but rather than employ a velocity of the lobe's expansion they use its age and size (for which $x_{e,3}/t_6 \equiv 1000 \text{ km s}^{-1}$ or $V_{rel,2} = 10$).

The Jet

A key component of this system is the jet. We use the relativistic relations given by Bicknell (1994) and Laing & Bridle (2002) to describe a jet of velocity V , rest mass density ρ , pressure p , enthalpy $w = u + p$ (where u is the internal energy density) and cross sectional area A . Ignoring buoyancy, we give general expressions and non-relativistic approximations for the momentum, energy, and mass fluxes, and a parameter which approximates the ratio of the jet's kinetic energy to its internal energy, R_{ke} :

$$\Pi = AV [\gamma^2 \rho V + \gamma^2 (w/c^2) V] \approx AV [\rho V + (w/c^2) V] \quad (\text{A34})$$

$$L = AV [\gamma(\gamma-1)\rho c^2 + \gamma^2 w] \approx AV [\frac{1}{2}\rho V^2 + w] \quad (\text{A35})$$

$$\dot{M} = AV \gamma \rho \approx AV \rho \quad (\text{A36})$$

$$R_{ke} = (\gamma-1)\rho c^2/w \approx \frac{1}{2}\rho V^2/w \quad (\text{A37})$$

where AV is the volume passing any given point per second, and $\beta = V/c$, $\gamma = (1-\beta^2)^{-1/2}$ are the usual relativistic velocity and Lorentz factors for the jet's bulk motion. In the current context we consider the jet to contain *two* components: (a) relativistic particles and fields with pressure P_{rel} , enthalpy $w = u + P_{rel} = 4P_{rel}$ and (usually negligible) rest mass density $\rho_{rel} \approx n_e m_p$ where n_e is given by Equation A24; and (b) a non-relativistic ('thermal') component of pressure P_{th} , enthalpy $w = (5/2)P_{th}$ and density ρ_{th} . We choose to characterize the relative amounts of these components using a filling factor, ff_{rj} , for the relativistic component. We further assume the two components are in rough pressure balance, $P_{th} \approx P_{rel} \equiv P$. Using j as subscript for the jet, we take for fiducials $P = 10^{-10} \text{ dyne cm}^{-2}$ ($\equiv 7.2 \times 10^5 \text{ K cm}^{-3}$ in P/k), $n_{th} = 1 \text{ cm}^{-3}$, $V_j = 10^3 \text{ km s}^{-1}$ and $A_j = 10^4 \text{ pc}^2$, where the latter area comes from the smallest resolved scale of the inner western jet, $A_{jet} \sim 0''.15 \times 0''.15 \cong 100 \text{ pc} \times 100 \text{ pc}$. Together these give:

$$\begin{aligned} \Pi_j &\approx A_j V_j [\rho_{th} V_j (1-ff_{rj}) + (P/c^2) V_j \frac{1}{2}(5+3ff_{rj}) + \rho_{rel} V_j ff_{rj}] \\ &\approx 1.6 \times 10^{33} (1-ff_{rj}) A_{j,4} V_{j,3}^2 n_{th} + 2.7 \times 10^{26} (1+0.6ff_{rj}) A_{j,4} V_{j,3}^2 P_{-10} + \\ &\quad 8.1 \times 10^{25} ff_{rj} A_{j,4} V_{j,3}^2 [X_0(\alpha_r)/aX_{0.5}(\alpha_r)] P_{-10}^{5/4} \text{ dyne} \end{aligned} \quad (\text{A38})$$

$$\begin{aligned} L_j &\approx A_j V_j [\frac{1}{2}\rho_{th} V_j^2 (1-ff_{rj}) + \frac{1}{2}P (5+3ff_{rj}) + \frac{1}{2}\rho_{rel} V_j^2 ff_{rj}] \\ &\approx 8.0 \times 10^{40} (1-ff_{rj}) A_{j,4} V_{j,3}^3 n_{th} + 2.5 \times 10^{39} (1+0.6ff_{rj}) A_{j,4} V_{j,3} P_{-10} + \\ &\quad 8.1 \times 10^{33} ff_{rj} A_{j,4} V_{j,3}^3 [X_0(\alpha_r)/aX_{0.5}(\alpha_r)] P_{-10}^{5/4} \text{ erg s}^{-1} \end{aligned} \quad (\text{A39})$$

$$\dot{M}_j \approx A_j V_j \rho_{th} (1-ff_{rj}) \approx 0.25 (1-ff_{rj}) A_{j,4} V_{j,3} n_{th} M_\odot \text{ yr}^{-1} \quad (\text{A40})$$

$$R_{ke} \approx \frac{\frac{1}{2}\rho_{th} V_j^2 (1-ff_{rj})}{\frac{1}{2}P (5+3ff_{rj})} \approx \frac{\Pi_j/A_j}{5P (1+0.6ff_{rj})} \approx \frac{20 \Pi_{j,33}/A_{j,4}}{P_{-10} (1+0.6ff_{rj})} \quad (\text{A41})$$

where we have ignored the contribution of ρ_{rel} in last two relations, A40 and A41. Note that if P is measured using a radio source then it hides and additional dependence on filling factor, and one should use: $P \equiv P_{ff=1} ff^{-4/7}$. Note also that for our parameter regime, as long as there is even a small thermal component, we can effectively ignore both the kinetic energy and the momentum of the relativistic component (but not its internal energy). Finally, the term $[X_0(\alpha_r)]/[X_{0.5}(\alpha_r)]$ spans a modest range 2.7 – 4.0 for the full range of observed spectral indices $\alpha_r = 0.6 - 0.8$. Note also that for a pure thermal jet $L_j/(c\Pi_j) = \frac{1}{2}\beta_j$, while for a pure relativistic jet $L_j/(c\Pi_j) \approx 1/\beta_j$, where $\beta_j = V_j/c$ (more exactly, from A38 and A39, $L_j/(c\Pi_j) = 1/\beta_j [(1 + \frac{1}{2}R_{rm}\beta_j^2)/(1 + R_{rm})]$ where R_{rm} is ratio of rest mass energy to enthalpy, $\rho_{rel}c^2/4P$, so the term in square brackets is of order unity for our parameter regime, using Equation A25).

Quantities used in the above relations have the following definitions:

cz , H_0 : redshift in km s^{-1} and Hubble constant in $\text{km s}^{-1} \text{Mpc}^{-1}$.

F_{5007} , $F_{H\beta}$, L_{5007} , $L_{H\beta}$: Reddening corrected [OIII] λ 5007 and $H\beta$ flux in $\text{erg s}^{-1} \text{cm}^{-2}$ and their associated luminosities in erg s^{-1} .

S_{60} , S_{100} : IRAS fluxes in Jy in the $60\mu\text{m}$, $100\mu\text{m}$ bands (1.11 and 1.13 for Mkn 78).

$h\nu_{H\beta}$, $\alpha_{H\beta}$, m_p : $H\beta$ photon energy = 4.09×10^{-12} erg; case B recombination coefficient for $H\beta$ at 10^4K = $3.0 \times 10^{-14} \text{cm}^{-3} \text{s}^{-1}$; proton mass in gm.

ϵ_H , ϵ_{low} , λ_{low} , α_o : Hydrogen ionization energy = 2.17×10^{-11} erg; low energy limit to the optical–UV–X-ray continuum absorbed by dust, in ergs and \AA (e.g. $\sim 4000\text{\AA}$); the power law spectral index for this continuum: $L_\nu \propto \nu^{-\alpha_o}$.

θ_{ex} , θ_{ey} , Δ_e , θ_{rx} , θ_{ry} , Δ_r : long and short diameters, in arcsec, of the [OIII] and radio regions, and their distance to the nucleus, in cm.

n_{em} , n_{ism} , n_{th} : proton density in cm^{-3} for the line emitting component, the ambient ISM, and the jet/wind thermal component.

V_{em} , W_{em} : [OIII] λ 5007 peak velocity and FWHM in km s^{-1} .

S_ν , λ , α_r , ν_1 , ν_2 : radio source flux in Jy at wavelength λ cm, with assumed power law $S_\nu \propto \nu^{-\alpha_r}$ between limits $\nu_1 = 0.01$ and $\nu_2 = 100 \text{GHz}$.

a , $X_0(\alpha_r)$, $X_{0.5}(\alpha_r)$, $X_{1.0}(\alpha_r)$: the factor specifying the relative contribution of energy in relativistic electrons and ions, $u_p = u_e + u_{ions} = au_e$, where we take $a = 2$ (equal energy in ions and electrons); the spectral shape function is defined by $X_q(\alpha) = (\nu_2^{q-\alpha} - \nu_1^{q-\alpha}) / (q - \alpha)$ with $\nu_1 = 0.01$ and $\nu_2 = 100$.

Fiducial values are quoted with the \log_{10} of the value specified, for example $V_{j,3}$ is V_j expressed in units of 10^3km s^{-1} .

APPENDIX

SLITLESS SPECTROSCOPY

In this appendix, we make a brief assessment of a potentially powerful STIS observing mode: “slitless spectroscopy”, since we have both good slit coverage and a deep (1700s) exposure using the G430M grating in slitless mode.

Clearly, this kind of data has both strengths and weaknesses. On the one hand, a single exposure captures information from the entire emission line region, in our case for all three emission lines $H\beta\lambda$ 4861, [OIII] $\lambda\lambda$ 4959, 5007. On the other hand, the information is convolved since spatial and velocity coordinates are superposed. Figure 5 shows our slitless data (top center), with the [OIII] direct PC image oriented to match the slitless image (top left). Contours of these two have been superposed (top right) by matching the bright emission region LW–1. In a general sense, it is clear from these images that the eastern side shows significant redshift, while parts of the western side seem to be blueshifted, consistent with an overall bipolar flow. With a sufficiently simple emission region, comprising well separated patches, it seems possible to identify which patch in the direct image corresponds with which patch in the slitless image, and thereby infer its velocity. Indeed, this approach has been adopted with good success in several studies (e.g. Kaiser et al. 2000; Ruiz et al. 2001).

The method does, however, seem to have its limitations. For example, even for simple emission regions, higher order information (e.g. linewidth, asymmetry, wings etc.) is usually unrecoverable, because of the confusion with nearby emission. With more complex emission regions ambiguities grow quickly as to which patch of emission in the direct image goes with which patch in the slitless image. Since we have good coverage with four slits, it is possible to reconstruct quite clearly how the slitless image has arisen. The lower six panels in Figure 5 show this, with the emission from each slit observation rebinned to simulate its location in the slitless image. The sum of all four slits is shown in the lowest right panel and many of its features can be found in the actual slitless image, while those that cannot can be traced to emission coming from between or outside the slits. Without attempting to describe these images in any detail, it is clear that in the absence of the slit data, it would be difficult to go beyond the simplest inferences from the slitless data, and even then genuine ambiguities would arise.

In an attempt to push the slitless method further, we considered what would be gained by taking several slitless images at different orientations (Becker 2000). This is formally equivalent to projecting the 3-d data set (RA, Dec, cz) onto a plane from several angles, and may therefore yield to tomographic reconstruction techniques. We simulated slitless observations from three orientations and used iterative back projection, and maximum entropy methods to try to reconstruct the original dataset. As might be expected, the problem is highly underconstrained and artifacts thoroughly confuse the reconstruction.

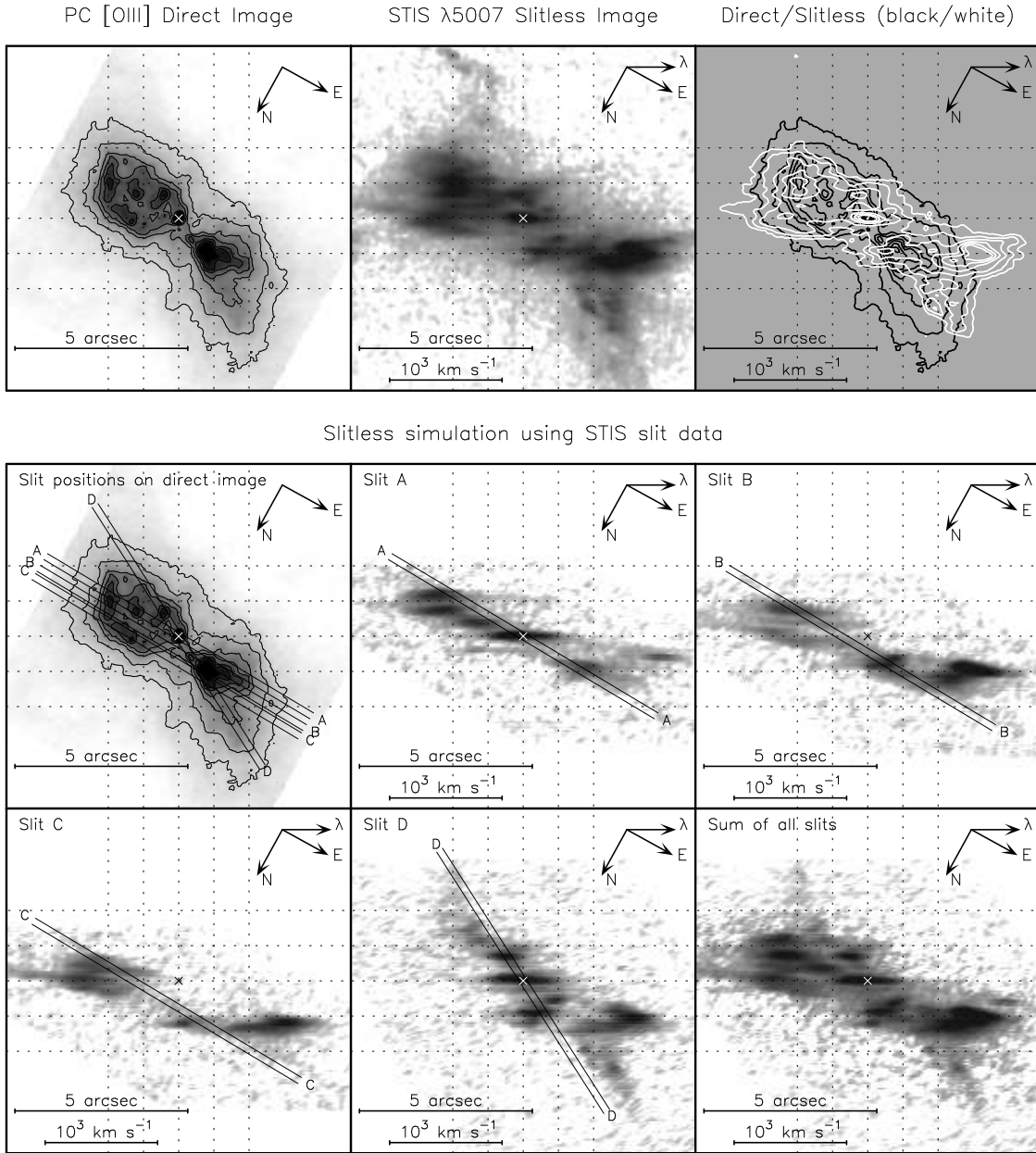


FIG. 5.— Slitless Spectroscopy. The top center panel shows the slitless [OIII] λ 5007 image taken with the G430M grating at an orientation of PA 151 and a horizontal dispersion axis (scales indicate 5 arcsec and 10^3 km s^{-1}). For reference, the top left panel shows the [OIII] λ 5007 PC direct image and the top right panel shows the two superimposed. The lower six panels present the STIS slit observations rotated to match the slitless observation, with their sum presented in the lower right panel. The various [OIII] velocity components are clearly visible and the sum matches quite well the observed slitless data. Without the slit data, however, interpreting the slitless data would be quite limited.

We conclude that by themselves, slitless images can provide simple but rather limited information. For complex objects (e.g. Mkn 78), even this information might prove to be quite ambiguous. Unfortunately, if detailed information is required, there seems to be no easy shortcut to using multiple slits.

REFERENCES

Becker, G.D. 2000, Undergraduate Thesis, University of Virginia
 Begelman, M.C. 1996, in *Cygnus A : Study of a Radio Galaxy*, Ed. C.L. Carilli, & D.A. Harris (Cambridge: Cambridge Univ. Press), 209
 Best, P.N., Carilli, C.L., Garrington, S.T., Longair, M.S., Rottgering, H.J.A. 1998, *MNRAS*, 299, 357
 Bicknell, G.V. 1994, *ApJ*, 422, 542
 Bicknell, G.V., Dopita, M.A., & O’Dea, C.P.O. 1997, *ApJ*, 485, 112
 Bicknell, G.V., Dopita, M.A., Tsvetanov, Z.I., & Sutherland, R.S. 1998, *ApJ*, 495, 68
 Binette, L., Wilson, A.S., & Storchi-Bergmann, T. 1996, *A&A*, 312, 365
 Blandford, R. D., & Eichler, D. 1987, *Phys. Rep.*, 154, 1
 Capetti, A., Axon, D.J., Macchetto, F., Marconi, A., Winge, C. 1999, *ApJ*, 516, 187
 Crenshaw, D.M., & Kraemer, S.B. 2000, *ApJ*, 532, L101
 de Bruyn, A.G., Wilson, A.S. 1978, *A&A*, 64, 433
 Dopita, M.A., & Sutherland, R.S. 1995, *ApJ*, 455, 468
 Falcke H., & Biermann P.L. 1995, *ã*, 293, 665
 Falcke, H., Wilson, A.S., & Simpson, C. 1998, *ApJ*, 502, 199
 Kaiser, M.E., et al. 2000, *ApJ*, 528, 260

- Laing, R.A., & Bridle, A.H. 2002, MNRAS, 336, 1161
- Laing, R. A., Parma, P., de Ruiter, H. R., & Fanti, R. 1999, MNRAS, 306, 513
- Miley, G.K. 1980, ARA&A, 18, 165
- Moffet, A.T. 1975, Stars and Stellar Systems, Vol. IX, p. 211. (Univ. Chicago Press)
- Nelson, C.H., & Whittle, M. 1996, ApJS, 99, 67
- Nelson, C.H., & Whittle, M. 1996, ApJ, 465, 96
- O'Dea, C.P. 1998, PASP, 110, 493
- Osterbrock, D.E. 1989, Astrophysics of Gaseous Nebulae and Active Galactic Nuclei (University Science Books)
- Ruiz, J.R. et al. 2001, AJ, 122, 2961
- Pedlar, A., Meaburn, J., Axon, D.J., Unger, S.W., Whittle, D.M., Meurs, E.J.A., Guerrine, N., & Ward, M.J. 1989, MNRAS, 238, 863
- Roy, A. L., Wilson, A. S., Ulvestad, J. S., & Colbert, J. M. 2000, Proceedings of the 5th European VLBI Network Symposium, Eds.: J.E. Conway, A.G. Polatidis, R.S. Booth & Y.M. Pihlstrm, (Onsala Space Observatory), 7
- Villar-Martn, M., Tadhunter, C., Morganti, R., Axon, D., Koekemoer, A. 1999, MNRAS, 307, 24
- Whittle, M. 1992a ApJ, 387, 109
- Whittle, M. 1992c ApJS, 79, 49
- Whittle, M., Pedlar, A., Meurs, E.J.A., Unger, S.W., Axon, D.J., & Ward, M.J. 1988, ApJ, 326, 125
- Whittle, M., & Wilson, A.S. 2004, AJ, 127, 606 (Paper I)
- Whittle, M., Rosario, D.J.V., Silverman, J.D., Nelson, C.H., & Wilson, A.S. 2004, AJ, submitted (Paper II).
- Wilson, A.S., & Willis, A.G. 1980, ApJ, 240, 429